Robust Nanogap Cluster Formation via Plasmonic Moiré Superlattices for Surface-Enhanced Raman Spectroscopy

Thesis by
Chiyoung Hwang

In Partial Fulfillment of the Requirements for
the Degree of
Doctor of Philosophy in Medical Engineering

CALIFORNIA INSTITUTE OF TECHNOLOGY
Pasadena, California

2026
(Defended May 15, 2026)

Chiyoung Hwang
ORCID: 0000-0003-4686-4683

ACKNOWLEDGEMENTS

Pursuing a Ph.D. in a new environment presented many challenges, but I am grateful to have reached this milestone and completed my degree.

First, I would like to express my sincere gratitude to my advisor, Professor Axel Scherer. Although I had little experience in nanofabrication before joining the group, his guidance and support enabled me to develop extensive knowledge and valuable hands-on experience in a wide range of fabrication techniques. I would also like to thank my thesis committee members, Professor Yu-Chong Tai, Professor Wei Gao, and Dr. Guy DeRose, for their time, thoughtful questions, and insightful comments during my defense.

My thanks also go to my colleagues in the Caltech Nanofabrication Group for their help and support, and to our laboratory administrative assistants, Kate Finigan and Joanne Pineda, for their continuous assistance throughout my doctoral studies.

In addition, I am deeply grateful to the staff members at the Kavli Nanoscience Institute for their expertise, support, and kindness. Their assistance was invaluable throughout my research and greatly contributed to the success of this work. I also gratefully acknowledge the Ilju Academic and Cultural Foundation for its financial support during my doctoral studies in the United States.

Lastly, I would like to express my deepest appreciation to my family and friends for their unwavering support and encouragement throughout this journey.

ABSTRACT

Plasmonic nanogaps enable strong confinement of electromagnetic fields and are central to a wide range of applications, including molecular sensing, spectroscopy, and quantum photonics. Achieving nanogaps with dimensions below 10 nm is particularly important for maximizing field enhancement, yet their reproducible fabrication remains difficult due to the sensitivity of conventional nanofabrication processes to small variations.

This thesis introduces a design strategy based on moiré superlattice geometry to generate nanogap clusters in a robust manner. By stacking two periodic nanodisk arrays with a small twist angle, a large-scale superlattice is formed, within which numerous ultranarrow gaps naturally arise from geometric effects. Numerical analysis shows that these gaps can be considerably smaller than the original structural features and can be formed consistently even in the presence of fabrication imperfections.

The proposed concept is validated experimentally through the fabrication of stacked nanodisk arrays using a sequential lithographic process. Voltage-contrast scanning electron microscopy is employed to verify the presence of electrically isolated nanogaps at the sub-10 nm level, providing clear evidence beyond conventional imaging methods. These results indicate that ultranarrow nanogaps can be realized without requiring extreme control over lithographic parameters.

Building upon this concept, elevated plasmonic moiré superlattices are further developed to enhance accessibility to field-enhancing regions, thereby improving sensing performance. The practical relevance of the proposed structures is demonstrated through surface-enhanced Raman spectroscopy measurements, which show consistently high signal enhancement across different fabrication conditions.

Taken together, this work presents a scalable and geometry-driven approach for the reliable creation of nanogap-rich plasmonic systems. The framework provides a versatile platform

for exploring nanoscale light–matter interactions and enables future developments in nanophotonic and sensing technologies.

PUBLISHED CONTENT AND CONTRIBUTIONS

C. Hwang and A. Scherer, “Plasmonic Moiré Superlattices for Robust Nanogap Cluster Formation,” *Small Methods* 10, no. 6 (2026): e02269. DOI: 10.1002/smtd.202502269

C.H. conceived the idea, performed numerical and experimental studies, and wrote the manuscript.

TABLE OF CONTENTS

LIST OF ILLUSTRATIONS AND/OR TABLES

Chapter 1

INTRODUCTION

This chapter is based on:

C. Hwang and A. Scherer, "Plasmonic Moiré Superlattices for Robust Nanogap Cluster Formation," *Small Methods* 10, no. 6 (2026): e02269. DOI: 10.1002/smtd.202502269

1.1 Optical Nanostructure-Based Biosensing and Raman Spectroscopy

Nanostructure-based biosensors have attracted considerable attention due to their ability to detect biological and chemical species with high sensitivity and precision [1–4]. Nanoscale architectures enhance interactions between analytes and sensing interfaces, enabling the detection of target molecules at low concentrations. Moreover, precise control of structural parameters at the nanoscale offers opportunities to improve both sensing performance and reproducibility. Among various sensing approaches, optical techniques are particularly attractive due to their label-free operation and high chemical specificity. Raman spectroscopy, in particular, has emerged as a powerful analytical tool, as it provides molecular fingerprint information based on vibrational modes of target molecules [5].

Raman scattering arises from the interaction between incident electromagnetic radiation and molecular vibrational and rotational states. By probing these vibrational and low-frequency modes, Raman spectroscopy enables non-destructive molecular identification with high specificity. Consequently, it has been widely applied across chemistry, materials science, biology, and medicine, as well as in structural analysis and in situ characterization of complex systems.

1.2 Mathematical Description of Raman Scattering

The classical Raman scattering process can be described by a simple analytical model by treating molecules in an electric field as induced electric dipoles [5]. The induced dipole moment μ of a molecule in an incident electric field E can be written as follows:

$$\mu = \alpha E,$$

$$E = E_0 \cos(\omega t),$$

where α denotes the polarizability of the molecule. In general, α is expressed as a tensor to account for anisotropic polarizabilities. The polarizability can be expanded as a Taylor series with respect to the vibrational normal coordinate Q:

$$\alpha = \alpha_0 + \left(\frac{\partial \alpha}{\partial Q}\right) Q + \cdots,$$

where α_0 is the static polarizability. The vibrational coordinate Q can be expressed as

$$Q = Q_0 \cos(\omega_m t),$$

where Q_0 and ω_m denote the amplitude and frequency of molecular vibration, respectively. Substituting these expressions into the dipole moment yields

$$\mu \cong \alpha_0 E_0 \cos(\omega t) + \left(\frac{\partial \alpha}{\partial Q}\right) E_0 Q_0 \cos(\omega_m t) \cos(\omega t)$$

$$= \alpha_0 E_0 \cos(\omega t) + \left(\frac{\partial \alpha}{\partial Q}\right)\left(\frac{E_0 Q_0}{2}\right) [\cos\{(\omega - \omega_m)t\} + \cos\{(\omega + \omega_m)t\}].$$

This expression indicates that the induced dipole radiates components at multiple frequencies. The first term corresponds to Rayleigh scattering, which is elastically scattered. The second and third terms correspond to Stokes and anti-Stokes Raman scattering, respectively. These

inelastically scattered components carry characteristic vibrational information about the molecules, enabling molecular fingerprinting.

1.3 Surface-Enhanced Raman Spectroscopy (SERS)

Despite its analytical strengths, conventional Raman spectroscopy suffers from an inherently small scattering cross-section. Only a small fraction of incident photons undergo inelastic scattering, resulting in low signal intensity under typical experimental conditions. This limitation significantly restricts the practical use of Raman spectroscopy, particularly for low-concentration analytes or nanoscale detection volumes. Overcoming this limitation has been a central challenge in the development of Raman-based sensing techniques.

Surface-enhanced Raman spectroscopy (SERS) addresses this limitation by exploiting strong electromagnetic field enhancement near plasmonic nanostructures [6–10]. When metallic nanostructures support localized surface plasmon resonances, collective oscillations of conduction electrons concentrate optical fields into subwavelength regions near the metal surface. Molecules located within these regions experience dramatically enhanced local fields, leading to orders-of-magnitude increases in Raman signal intensity. This plasmonic enhancement mechanism forms the physical foundation of SERS, enabling highly sensitive molecular detection, in some cases down to the single-molecule level.

1.4 Electromagnetic Mechanism of SERS

In SERS, the dominant contribution arises from the strong electromagnetic interaction between the incident optical field and the molecules, resulting in enhanced radiation from induced molecular dipoles. In addition, further enhancement can arise from charge-transfer interactions between the molecule and a nearby surface, which alter the electronic structure of the molecule and enhance the Raman scattering probability. While both mechanisms can contribute to signal enhancement, the electromagnetic mechanism [11, 12] is generally regarded as the primary source of strong Raman signal amplification in plasmonic systems.

When localized surface plasmons are excited, highly confined electromagnetic fields are generated in nanoscale regions, often referred to as hotspots. The Raman enhancement can be described as a two-fold process, in which both the incident and Raman-scattered fields are amplified, resulting in an overall enhancement that scales approximately with the fourth power of the local electric field amplitude [11, 12]. This strong dependence highlights the importance of generating highly localized electromagnetic fields for achieving high SERS sensitivity. Accordingly, extensive efforts have been devoted to designing plasmonic structures for efficient SERS applications, including periodically arranged nanostructures, structures with sharp geometric features, and architectures incorporating extremely small nanogaps.

1.5 Technical Challenges in Realizing Sub-10 nm Plasmonic Nanogap Structures

Among various plasmonic nanostructures, nanogaps are particularly effective in generating highly confined electromagnetic fields and broadband optical enhancement [13–20]. Nanometer-scale separations between closely spaced metallic nanostructures can host extremely localized electromagnetic hotspots, where the local field intensity is maximized. Despite these attractive properties, the reliable fabrication of plasmonic nanogaps with sub-10 nm dimensions remains a significant challenge. Existing fabrication methods can generally be categorized into bottom-up and top-down approaches. Bottom-up approaches, such as nanoparticle self-assembly and colloidal lithography, can provide highly dense nanogap distributions over large areas with relatively low fabrication cost [16–20]. However, these approaches often suffer from limited controllability and reproducibility in gap geometry, spatial arrangement, and hotspot distribution. In contrast, top-down approaches, including electron-beam lithography (EBL), focused ion beam milling, interference lithography, and edge lithography, offer superior structural controllability, alignment accuracy, and design flexibility [16–20]. Although top-down methods generally involve lower throughput and higher fabrication complexity, they are more suitable for reliably realizing engineered plasmonic nanogap structures. Representative fabrication approaches and their characteristics are summarized in Table 1.1 [16–20].

Table 1.1 Representative fabrication methods for sub-10 nm plasmonic nanogap structures.

Fabrication method	Approach	Typical gap size	Advantages	Limitations
Nanoparticle self-assembly	Bottom-up	<5 nm	Extremely small gaps, large-area hotspot formation, low-cost	Limited control over geometry and reproducibility
Nanosphere / colloidal lithography	Bottom-up	~10 nm	Scalable, inexpensive, high-density periodic structures	Limited pattern flexibility and alignment control
Electron-beam lithography	Top-down	~10 nm	High-resolution, arbitrary pattern design, reliable alignment	Low throughput, complex process optimization
Focused ion beam milling	Top-down	Few nm	Direct nanoscale patterning, high spatial precision	Ion-induced damage and contamination
Edge lithography / shadow evaporation	Top-down	Sub-10 nm	Reliable ultranarrow gaps, relatively simple geometry control	Limited pattern geometries
Interference lithography / EUV-based methods	Top-down	Sub-10 nm	Large-area periodic nanopatterning	High system complexity and cost

Extensive efforts have been devoted to developing various top-down fabrication methods for plasmonic structures featuring dense and well-controlled nanogaps [21–30]. Nanogap fabrication methods based on EBL are among the most widely used and reliable approaches due to their exceptional resolution in patterning, despite their intrinsically low throughput [23–30]. However, even with EBL, the reliable formation of nanogap clusters incorporating sub-10 nm gaps remains challenging. Specifically, achieving such ultranarrow gaps requires meticulous optimization of multiple lithographic parameters, including beam current, exposure dose, resist type and thickness, development conditions, and proximity effect correction [30–34].

Figure 1.1 shows an array of nanogaps illustrating the fabrication inconsistencies discussed above. The nanogaps were designed to be identical, with a gap spacing of 10 nm between the electrode tips. To pattern the nanogap structures, EBL was performed using a 50-nm-thick polymethyl methacrylate (PMMA) electron-beam resist layer deposited on a silicon nitride (SiN) substrate. After PMMA development, 3 nm titanium (Ti) and 6 nm gold (Au) were sequentially deposited, followed by metal lift-off. Scanning electron microscopy (SEM) images show that some nanogaps are significantly larger than the designed spacing, while others are smaller than intended, and some are not even open, resulting in electrically connected electrodes.

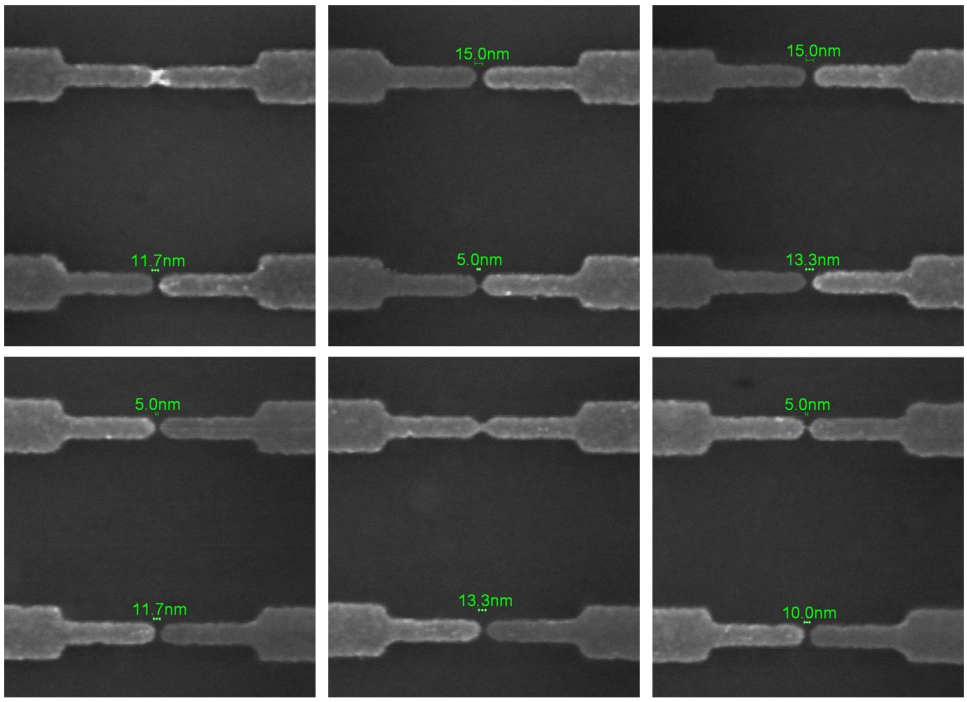

Figure 1.1 Scanning electron microscopy (SEM) images of a nanogap array fabricated by electron-beam lithography (EBL). A designed gap spacing between the electrode tips was 10 nm. The images reveal fabrication inconsistencies in nanogap formation, where some gaps are larger than the designed spacing, while others are smaller than intended, and some are closed, leading to electrically connected electrodes. This variability highlights the difficulty of reliably fabricating ultranarrow nanogaps even with state-of-the-art lithographic approaches.

This example demonstrates that small variations in fabrication parameters can lead to significant changes in the final gap size, particularly for ultranarrow gaps at the few-nanometer scale. As a result, the formation of dense nanogap clusters with uniform sub-10 nm gaps remains challenging to reproduce over large areas. Furthermore, cumulative alignment errors and patterning imperfections become increasingly critical as the target gap size approaches the intrinsic resolution limit of the lithographic process. These challenges highlight the need for alternative strategies that can generate ultranarrow nanogaps in a manner that is less sensitive to fabrication variability and process imperfections.

1.6 Photonic Moiré Structures for Nanogap Applications

Alongside advances in plasmonic nanostructures, photonic moiré superlattices have emerged as a powerful platform in photonics and nanophotonics [35–47]. Moiré structures are formed by stacking periodic lattices with a small relative twist angle or lattice mismatch, giving rise to long-range superlattice patterns with new symmetry and length scales. Such configurations have enabled a wide range of exotic optical phenomena, including tunable light modulation [36–38], wavefront shaping [39–41], hyperbolic metasurfaces [42], chiroptical metamaterials [43], and lasing based on photonic flatbands [44–47]. The distinct nature of moiré structures provides a unique route to engineering optical functionality.

Motivated by these developments, this thesis explores the application of moiré superlattice concepts to nanogap-based plasmonic sensing. By leveraging the intrinsic geometric properties of moiré structures, this thesis aims to generate dense clusters of plasmonic nanogaps in a manner that is robust against typical fabrication imperfections. The central hypothesis is that moiré-induced geometric amplification enables the reliable formation of ultranarrow nanogaps and their large-area realization, thereby addressing key limitations of conventional nanogap-based SERS substrates. Through numerical analysis, nanofabrication, and experimental characterization, this work investigates the underlying principles, fabrication strategies, and sensing performance of plasmonic moiré superlattices as a new platform for surface-enhanced Raman spectroscopy.

1.7 Organization of the Thesis

The remainder of this thesis is organized as follows. Chapter 2 introduces the concept of geometry-driven nanogap cluster formation in moiré superlattices and presents numerical analyses based on the superposition of periodic nanodisk arrays. Chapter 3 describes the experimental realization of plasmonic moiré superlattices through the stacking of two twisted hexagonal nanodisk arrays and verifies the formation of sub-10 nm gaps using voltage-contrast SEM [48–52]. Chapter 4 extends this approach to elevated plasmonic moiré

structures and evaluates their performance as surface-enhanced Raman spectroscopy substrates. Finally, Chapter 5 summarizes the main findings of this thesis and discusses further characterization and possible directions for improving and extending plasmonic moiré superlattices.

Chapter 2

PRINCIPLES OF GEOMETRY-DRIVEN NANOGAP FORMATION IN MOIRÉ SUPERLATTICES

This chapter is based on:

C. Hwang and A. Scherer, "Plasmonic Moiré Superlattices for Robust Nanogap Cluster Formation," *Small Methods* 10, no. 6 (2026): e02269. DOI: 10.1002/smtd.202502269

In this chapter, the principle of geometry-driven nanogap formation in plasmonic moiré superlattices is introduced and systematically investigated through numerical analysis. The spatial distribution, alignment characteristics, and parameter dependence of nanogap clusters are examined to provide a comprehensive understanding of their formation mechanisms.

2.1 Concept and Analytical Framework of Geometry-Driven Nanogap Formation in Moiré Superlattices

Figure 2.1a illustrates a conceptual fabrication scheme for a plasmonic moiré superlattice designed to validate the proposed approach, in which two periodic nanodisk arrays are stacked on a dielectric-coated metal substrate. The fabrication process comprises two steps [27–29], each involving lithography, metal deposition, and lift-off. The second lithography step requires rotational alignment to control the size of the moiré superlattice primitive cells, thereby determining the dimensions of the resulting nanogap clusters.

Geometric parameters and structural conditions are defined for the numerical analysis of nanogap generation in the proposed structure. Figure 2.1b shows a schematic of the nanodisk arrangement in the moiré structure. In this study, two identical hexagonal nanodisk arrays serve as the constituent layers, referred to as Array 1 and Array 2. For each array, the nanodisk diameter and the center-to-center spacing are denoted as D and S, respectively. The relative twist angle is denoted by α, and the lateral offsets of Array 2 relative to Array 1 are

denoted as L_x and L_y. The nanogap alignment angle φ is defined as the angle between the x-axis and the line connecting the centers of a nanodisk pair forming a nanogap, ranging from 0° to 180°. For analytical convenience, Array 1 is assumed to be infinitely extended, ensuring that all nanodisks in Array 2 are fully embedded in Array 1.

Figure 2.1c shows a schematic of the procedure used to identify nanogaps smaller than a threshold g, where g denotes the maximum gap width considered. A coordinate transformation is applied to determine the center positions of the nanodisks in Array 2 in the x–y coordinate system using the following equation:

$$\begin{pmatrix} x \\ y \end{pmatrix} = \begin{pmatrix} \cos\alpha & -\sin\alpha \\ \sin\alpha & \cos\alpha \end{pmatrix} \begin{pmatrix} x' \\ y' \end{pmatrix} + \begin{pmatrix} L_x \\ L_y \end{pmatrix}.$$

Each nanodisk in Array 2 is then mapped into a rectangular unit cell centered at the origin using the background periodicity of Array 1. Based on this mapping, nanogap widths between the mapped nanodisk and the seven surrounding nanodisks in Array 1 are computed to identify nanogaps satisfying the threshold condition. Note that this procedure requires the geometric constraint $D + g < S\sqrt{3}/2$ to be satisfied, ensuring that only these seven nanodisks are involved in sub-g nanogap formation.

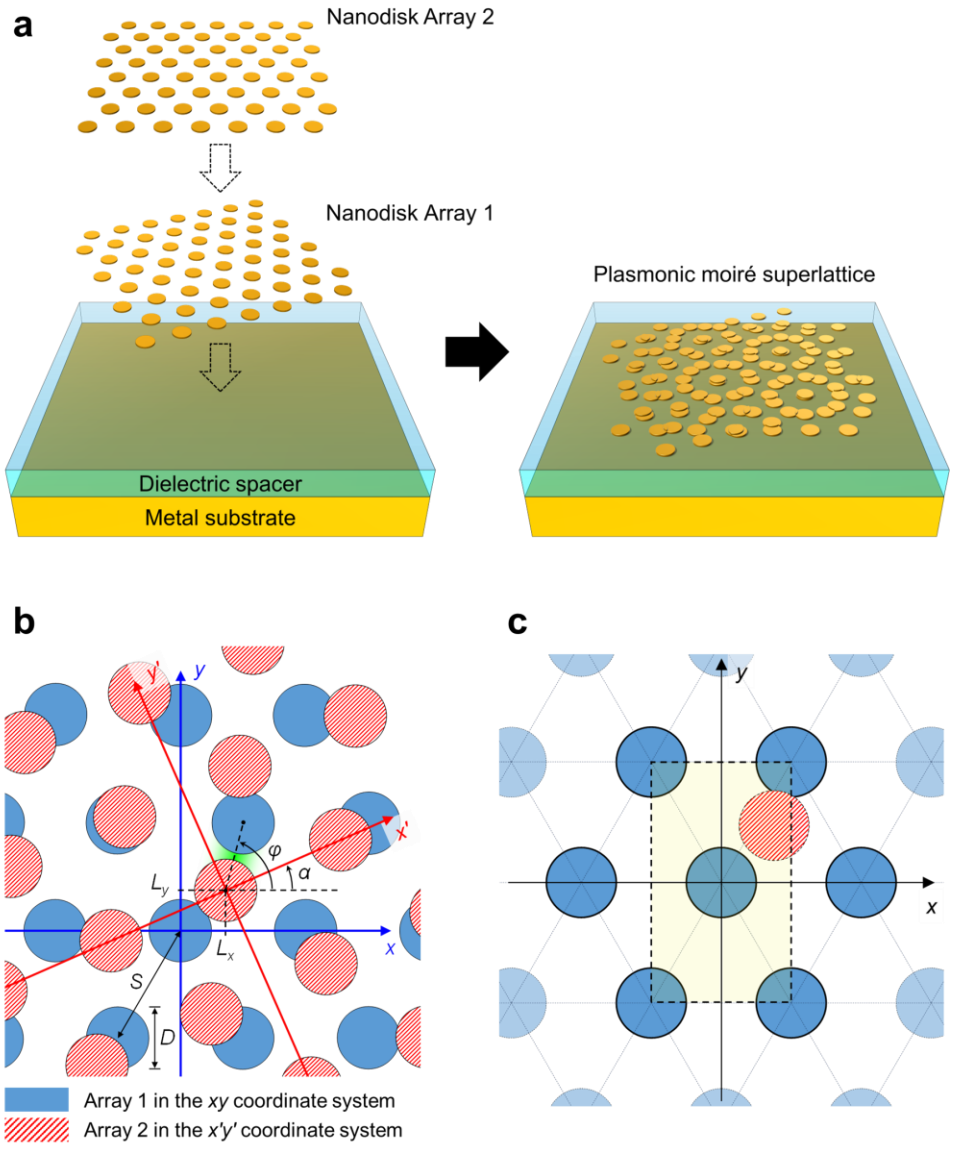

Figure 2.1 Conceptual overview of the geometry-driven nanogap formation in plasmonic moiré superlattices and the corresponding analytical framework. (a) Schematic illustration of plasmonic moiré superlattices created through the stacking of two twisted periodic nanodisk arrays. (b) Arrangement of stacked nanodisks and associated parameters. (c) Schematic representation of the procedure for counting target nanogaps for a nanodisk in Array 2, assuming the geometric condition that nanogaps are formed exclusively with the seven nanodisks in Array 1 surrounding the unit cell (indicated by the dotted rectangular box).

2.2 Numerical Analysis of Nanogap Cluster Formation and Spatial Distribution

Based on the defined geometric configurations, the formation of nanogap clusters in the moiré superlattice is numerically investigated. Figures 2.2a–c present moiré superlattice patterns generated by stacking two twisted hexagonal nanodisk arrays with D = 250, 300, and 350 nm, respectively, at fixed values of S = 600 nm and $\alpha = 2°$. Although the simulation is purely geometric and dimensionless, the results are expressed in length units for consistency with experimental conditions. As observed in Figures 2.2a–c, the size of the superlattice primitive cell is independent of D when S and α are fixed. The enlarged regions reveal a large number of non-overlapping nanodisks in the intermediate areas between adjacent primitive cells, leading to the formation of nanogap clusters.

To further analyze nanogap formation, nanodisks in Array 2 that form sub-10, sub-20, and sub-30 nm gaps with adjacent nanodisks in Array 1 are identified, as shown in Figures 2.2d–f for D = 250, 300, and 350 nm, respectively. The spatial distributions of these nanodisks show that clusters of nanogaps, including those below 10 nm, can emerge simply by stacking two periodic arrays, despite the much larger nanodisk size and spacing in each array. Moreover, the nanogap-forming nanodisks are distributed in ring-shaped regions that closely align with the boundaries of the moiré superlattice primitive cells when $S = 2D$. When $S < 2D$, the circular bands expand outward, whereas for $S > 2D$, they contract inward. The angular orientation φ of each nanogap is represented by the color of each nanodisk in Figures 2.2d–f. The calculated angles indicate a clear tendency for nanogap alignment to be nearly orthogonal to the radial direction from the center of the primitive cell.

These findings suggest that locally dense nanogap clusters can be realized using conventional lithography techniques with patterning feature sizes much larger than the target gap width, provided that rotational alignment is controlled with reasonable precision. In addition, the directional regularity provides a practical advantage by enabling the estimation of nanogap orientations through observation of the substantially larger primitive cells, without the need to resolve individual nanodisks using high-resolution nanoscale microscopy.

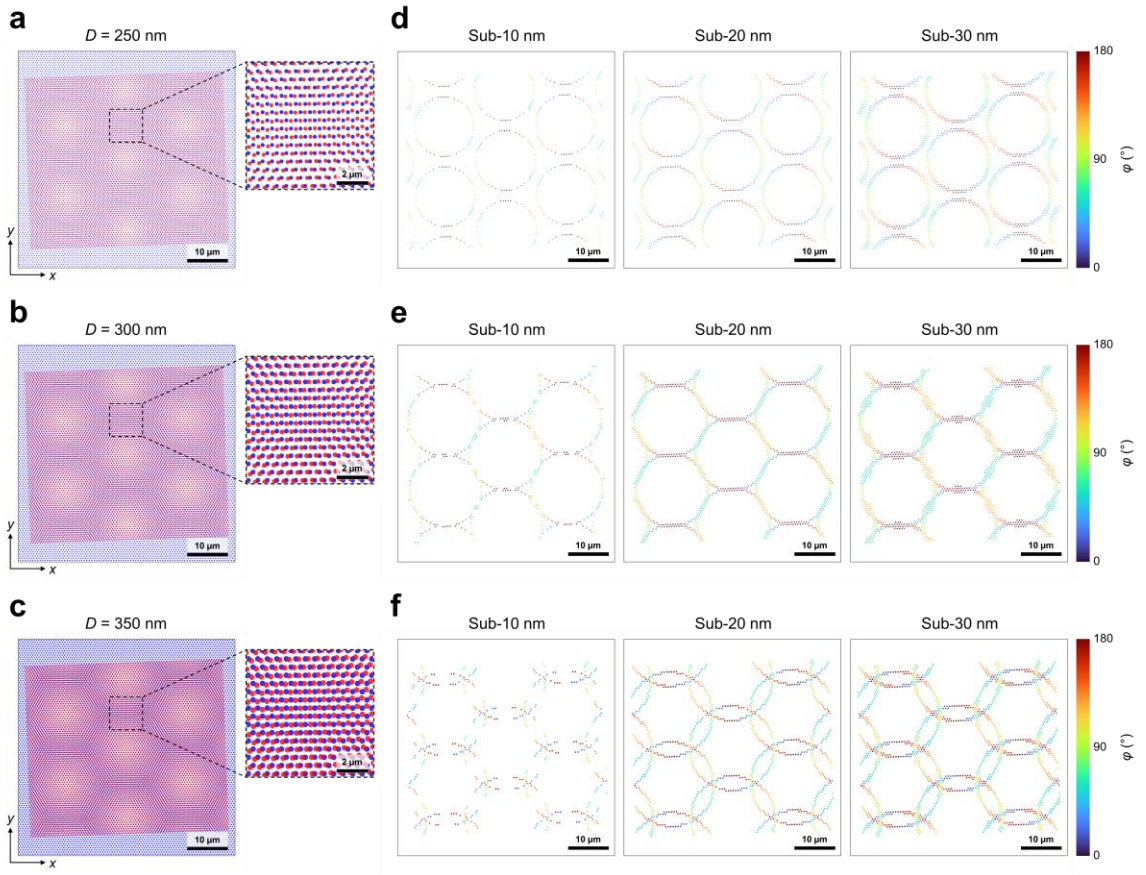

Figure 2.2 Numerical demonstration of geometry-driven nanogap cluster formation and their spatial and angular distributions in plasmonic moiré superlattices. Calculated moiré superlattice patterns for D = 250, 300, and 350 nm shown in (a), (b), and (c), respectively, with fixed parameters of S = 600 nm and α = 2°. (d–f) Corresponding maps of nanodisks in Array 2 that participate in forming sub-10 nm, sub-20 nm, and sub-30 nm gaps, respectively. The angular orientation φ of each nanogap is encoded by the color of the corresponding nanodisk. The average alignment angles are indicated for nanodisks that form two nanogaps.

2.3 Geometric Conditions for Multiple Nanogap Formation

From the spatial distributions of nanodisks in the nanogap cluster region (see Figures 2.2a–c), it is evident that multiple nanogaps can form around a single nanodisk. Figure 2.3 illustrates color-coded regions in Array 1 that correspond to the formation of one, two, and

three sub-g gaps, depending on the position of a nanodisk center in Array 2, where g denotes the maximum nanogap size considered. These regions are defined by the condition that the center-to-center distance between adjacent nanodisks lies between $2D$ and $2D + g$. Geometric analysis shows that three sub-g gaps can form around a nanodisk when $S/\sqrt{3} - g < D < S/\sqrt{3}$. This condition is not satisfied under the parameters used in this study.

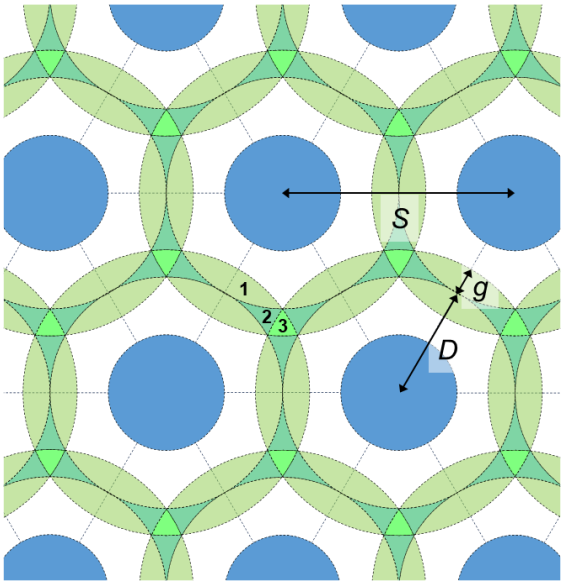

Figure 2.3 Schematic illustration of spatial regions associated with the formation of multiple nanogaps around a single nanodisk. Color-coded regions in Array 1 indicate where a nanodisk in Array 2 forms one, two, or three sub-g gaps, depending on its position, where g denotes the maximum gap width considered.

2.4 Definition of Average Nanogap Alignment Angle

To visualize the spatial distribution of nanogap-forming nanodisks, alignment angles ranging from 0° to 180° are color-coded on the nanodisks in Array 2. When a nanodisk forms two nanogaps, an average nanogap alignment angle is assigned to represent its angular characteristics. This average angle is defined as illustrated in Figure 2.4.

For the three possible cases shown in Figure 2.4, the average alignment angle is determined as follows. When the difference between the two angles is smaller than 90°, a simple arithmetic average is used:

$$\varphi_{avg} = (\varphi_1 + \varphi_2)/2.$$

When the difference between the two angles and their arithmetic average are both larger than 90°, the average alignment angle is defined as

$$\varphi_{avg} = (\varphi_1 + \varphi_2)/2 - 90°.$$

When the difference between the two angles is larger than 90° but the arithmetic average is smaller than 90°, the average alignment angle is defined as

$$\varphi_{avg} = (\varphi_1 + \varphi_2)/2 + 90°.$$

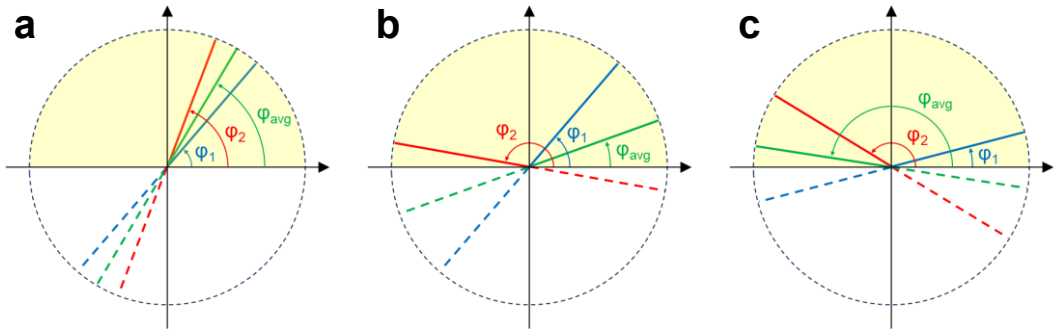

Figure 2.4 Definition of the average nanogap alignment angle for nanodisks forming two nanogaps. Three possible cases are considered depending on the angular difference between the two nanogaps: (a) when the difference is smaller than 90°, the average angle is given by $\varphi_{avg} = (\varphi_1 + \varphi_2)/2$; (b) when both the difference and the arithmetic average exceed 90°, the average angle is defined as $\varphi_{avg} = (\varphi_1 + \varphi_2)/2 - 90°$; (c) when the difference is larger than 90° but the arithmetic average is smaller than 90°, the average angle is defined as $\varphi_{avg} = (\varphi_1 + \varphi_2)/2 + 90°$.

2.5 Effect of Lateral Offsets on Nanogap Cluster Distribution

In the numerical calculations shown in Figure 2.2, the lateral offsets of Array 2 (L_x and L_y) are set to zero, since they primarily affect the spatial positioning of nanogaps. The effect of lateral offsets on the spatial distribution of nanogap-forming nanodisks is investigated in Figure 2.5. Dashed boxes, indicating the enlarged nanogap-rich regions shown in Figures 2.2a–c, are displayed in all subfigures to aid comparison and to emphasize the changes resulting from the applied offsets. The results show that nanogap clusters shift vertically with changes in L_x, whereas they shift horizontally with changes in L_y.

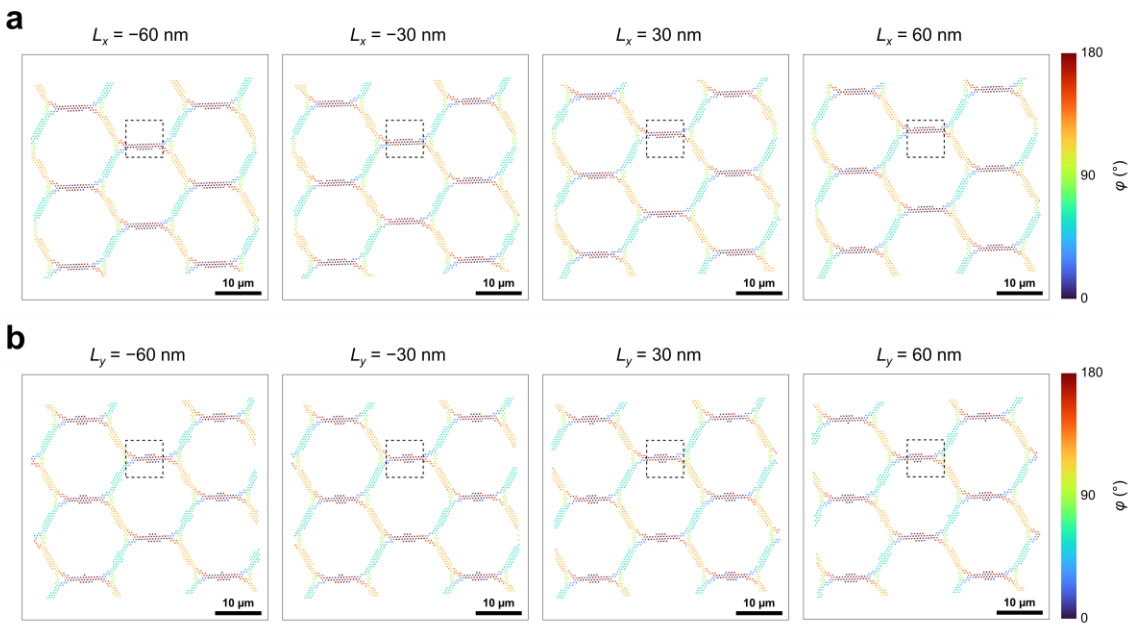

Figure 2.5 Effect of lateral offsets on the spatial distribution of nanogap-forming nanodisks in plasmonic moiré superlattices. Numerically calculated spatial distributions of sub-30 nm nanogap-forming nanodisks in Array 2 and their corresponding nanogap alignment angles (φ) for (a) $L_x = -60$, -30, 30, and 60 nm with fixed $L_y = 0$, and for (b) $L_y = -60$, -30, 30, and 60 nm with fixed $L_x = 0$, demonstrating the effects of lateral offsets applied to Array 2 along the x- and y-directions, respectively. The other parameters are kept constant at $S = 600$ nm, $D = 300$ nm, and $\alpha = 2°$. Dashed boxes, indicating the enlarged nanogap-rich regions shown in Figures 2.2a–c, are displayed in all subfigures to aid comparison and to emphasize the changes resulting from the applied offsets.

2.6 Geometric Interpretation and Parameter Dependence of Nanogap Cluster Formation

The nanogap-forming behavior can be understood by examining the size of the superlattice primitive cells and the arrangement of nanodisks near their interfaces. Figure 2.6a provides a schematic (not to scale) illustrating two adjacent primitive cells and the corresponding nanodisks from each array at the interface, specifically for the case of $S = 2D$ under a small twist angle. For clarity, thirteen nanodisks from Array 1 and five from Array 2 are explicitly depicted. The actual nanodisk distribution within each primitive cell may slightly deviate

from the illustration due to the aperiodic nature of the moiré superstructure. The distance between the centers of two adjacent primitive cells, denoted as Λ, is given by $\Lambda = S/\{2\sin(\alpha/2)\}$. For small twist angles, this can be approximated as $\Lambda \approx S/\alpha$. Accordingly, the angle θ, defined by two line segments extending from the center of a primitive cell to the centers of two adjacent nanodisks in Array 1, can be approximated as $\theta \approx 2\alpha$ based on geometric considerations. This implies that, near the midpoint of the line connecting the centers of two adjacent primitive cells, the nanodisks adopt an interleaved configuration. On either side of the interface, the nanodisk pairs show larger or smaller inter-disk gaps, resulting in widened separations or partial overlaps. This explains why the ring-shaped nanogap cluster region deviates from the zone defined by $S = 2D$, expanding when $S < 2D$ and contracting when $S > 2D$. It can be readily shown that the effective radius of the ring-shaped nanogap cluster band is approximated as $R_{NC} = (D/S)\Lambda$, based on the schematic shown in Figure 2.6b.

The robustness of nanogap generation in the moiré-based configuration can be assessed through a quantitative numerical analysis of how *D* and *S* influence the resulting nanogap count. Figures 2.6c and 2.6d show the normalized nanogap count, defined as the average number of nanogaps per nanodisk in Array 2, plotted as a function of *D* and *S*, respectively. In Figures 2.6c and 2.6d, *S* and *D* are fixed at 600 and 300 nm, respectively. The five curves in each plot correspond to different target nanogap widths. Here, Array 2 consists of a sufficiently large number of nanodisks (5001 × 5001), ensuring statistical convergence regardless of lateral offsets. As shown in Figure 2.6c, the normalized nanogap count increases linearly with *D* at fixed *S*, with curves corresponding to smaller nanogaps exhibiting more gradual slopes. Conversely, Figure 2.6d shows that the normalized nanogap count is inversely proportional to *S* at fixed *D*. This behavior arises because nanogap clusters approximately occupy ring-shaped regions, and the area of a circular band with a fixed width increases linearly with its radius. The overall yield of sub-10 nm gaps does not show a strong dependence on variations in *D* and *S*, and nanogaps of various widths can still be produced over a wide parameter range.

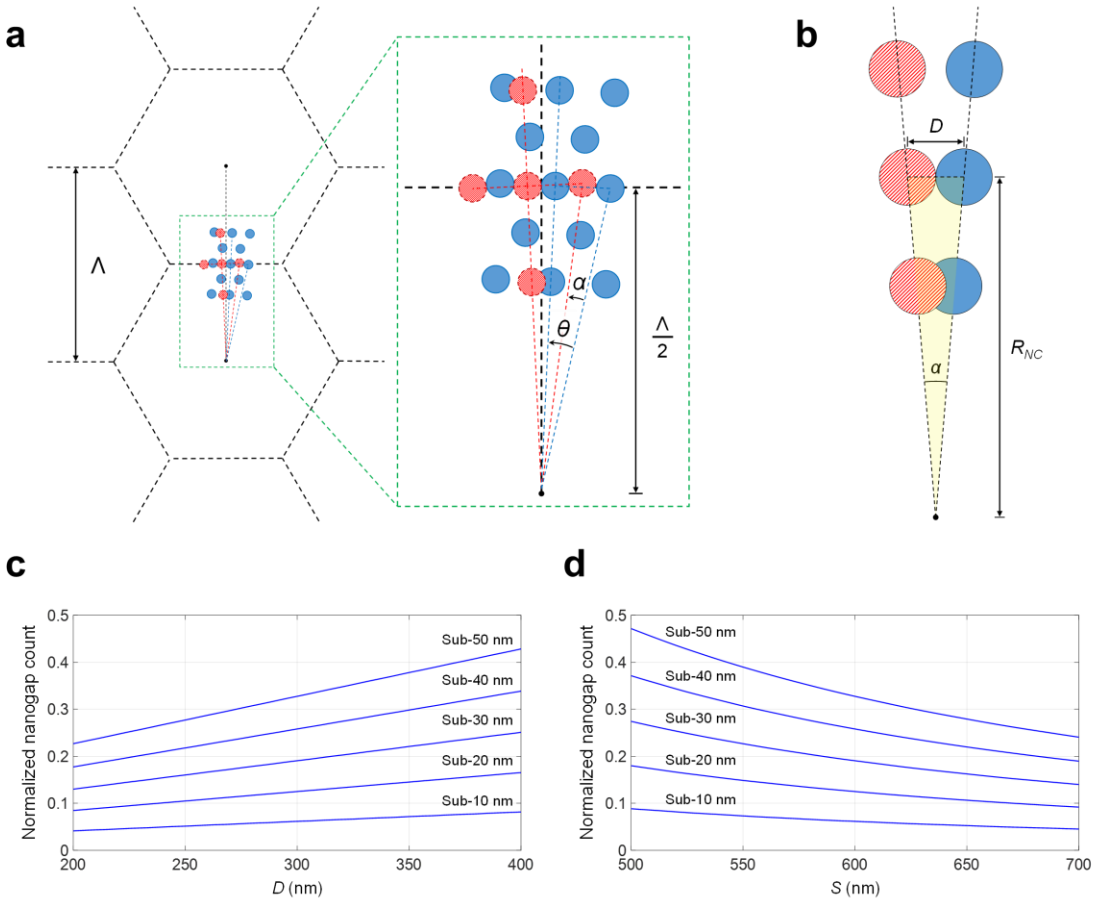

Figure 2.6 Geometric interpretation and parameter dependence of nanogap cluster formation in plasmonic moiré superlattices. (a) Conceptual diagram of nanogap cluster formation along the interface between adjacent superlattice primitive cells under the condition $S = 2D$, illustrating the geometrically induced proximity between nanodisks. Dashed hexagons represent the primitive cells. (b) Diagram showing nanodisks near the line segment connecting two primitive cell centers, from which the effective radius of the ring-shaped nanogap cluster is derived. (c) Normalized nanogap count as a function of D (200–400 nm) at fixed $S = 600$ nm. (d) Normalized nanogap count as a function of S (500–700 nm) at fixed $D = 300$ nm. For (c) and (d), all other parameters are fixed at $L_x = L_y = 0$ and $\alpha = 2°$.

Chapter 3

EXPERIMENTAL VALIDATION OF NANOGAP CLUSTER FORMATION IN PLASMONIC MOIRÉ SUPERLATTICES

This chapter is based on:

C. Hwang and A. Scherer, "Plasmonic Moiré Superlattices for Robust Nanogap Cluster Formation," *Small Methods* 10, no. 6 (2026): e02269. DOI: 10.1002/smtd.202502269

In this chapter, the proposed concept of nanogap cluster formation, including sub-10 nm nanogaps, is experimentally validated through the realization of plasmonic moiré superlattices generated by stacking two periodic arrays of Au nanodisks on a planar substrate. Electrical isolation of the fabricated nanogaps is verified using voltage-contrast SEM, and the corresponding plasmonic field enhancement is evaluated through full-wave electromagnetic simulations.

3.1 Fabrication of Plasmonic Moiré Superlattices

Figure 3.1 presents SEM images of three plasmonic moiré superlattice samples. All samples share nominal fabrication parameters of S = 600 nm and α = 2°, but differ in D, which was set to 250, 300, and 350 nm for Figures 3.1a–c, respectively. As illustrated in Figure 2.1a, each sample was fabricated by sequentially stacking two hexagonal nanodisk arrays on a 200-nm-thick alumina (Al_2O_3) layer deposited on an Au substrate. The alumina-coated metal substrate was fabricated by sequential deposition of a 10 nm Ti adhesion layer, 100 nm Au, and 200 nm alumina on a single-side-polished silicon (Si) substrate using magnetron sputtering (ATC Orion 8, AJA International). A moiré superlattice was fabricated on the alumina layer by stacking two periodic Au nanodisk arrays (401 × 401 elements for each array). For each nanodisk array, a 3-nm-thick Ti adhesion layer and a 30-nm-thick Au layer

were sequentially deposited. This process involved two cycles of EBL, metal deposition, and lift-off.

Each cycle began with spin-coating a 200-nm-thick layer of 950K PMMA onto the sample, followed by baking at 180 °C for 4 min. Electron-beam writing was performed using a Raith EBPG 5000+ system operated at 100 keV, with a beam current of 1 nA and an exposure dose of 800 $\mu C \cdot cm^{-2}$. Proximity effect correction was performed using the software tools BEAMER and TRACER (GenISys GmbH). The exposed PMMA was developed in a 1:3 mixture of methyl isobutyl ketone (MIBK) and isopropyl alcohol (IPA) for 60 s, followed by rinsing with IPA for 10 s and drying under nitrogen. Subsequently, a 3-nm-thick Ti layer and a 30-nm-thick Au layer were deposited by electron-beam evaporation (ATC Orion, AJA International) at deposition rates of 0.5 and 1 $Å \cdot s^{-1}$ for Ti and Au, respectively. During deposition, the chamber pressure was maintained at a level on the order of 10^{-8} Torr. The metal lift-off process was performed in acetone, followed by rinsing with IPA and drying under nitrogen. During the second EBL, rotational alignment was performed to achieve the target twist angle of 2°, while translational alignment was constrained less strictly, provided that the two arrays were adequately superimposed.

In each panel of Figure 3.1, the left image shows the primitive cell structures, while the middle image highlights the nanogap cluster region where the smallest gaps are observed. The observed dimensions of the superlattice primitive cells confirm that the rotational alignment during the second EBL was successfully achieved. The high-magnification images on the right reveal sub-10 nm gaps within these clusters, demonstrating the formation of extremely narrow nanogaps. Consistent with the numerical results shown in Figure 2.2, the smallest nanogaps are located along the boundaries of the superlattice primitive cells for D = 300 nm. In contrast, for D = 250 and 350 nm, the regions containing the smallest gaps are slightly shifted away from these boundaries. SEM images were acquired in secondary electron mode using a Nova 600 NanoLab system (FEI). The electron-beam accelerating voltage and probe current were set to 5 kV and 400 pA, respectively.

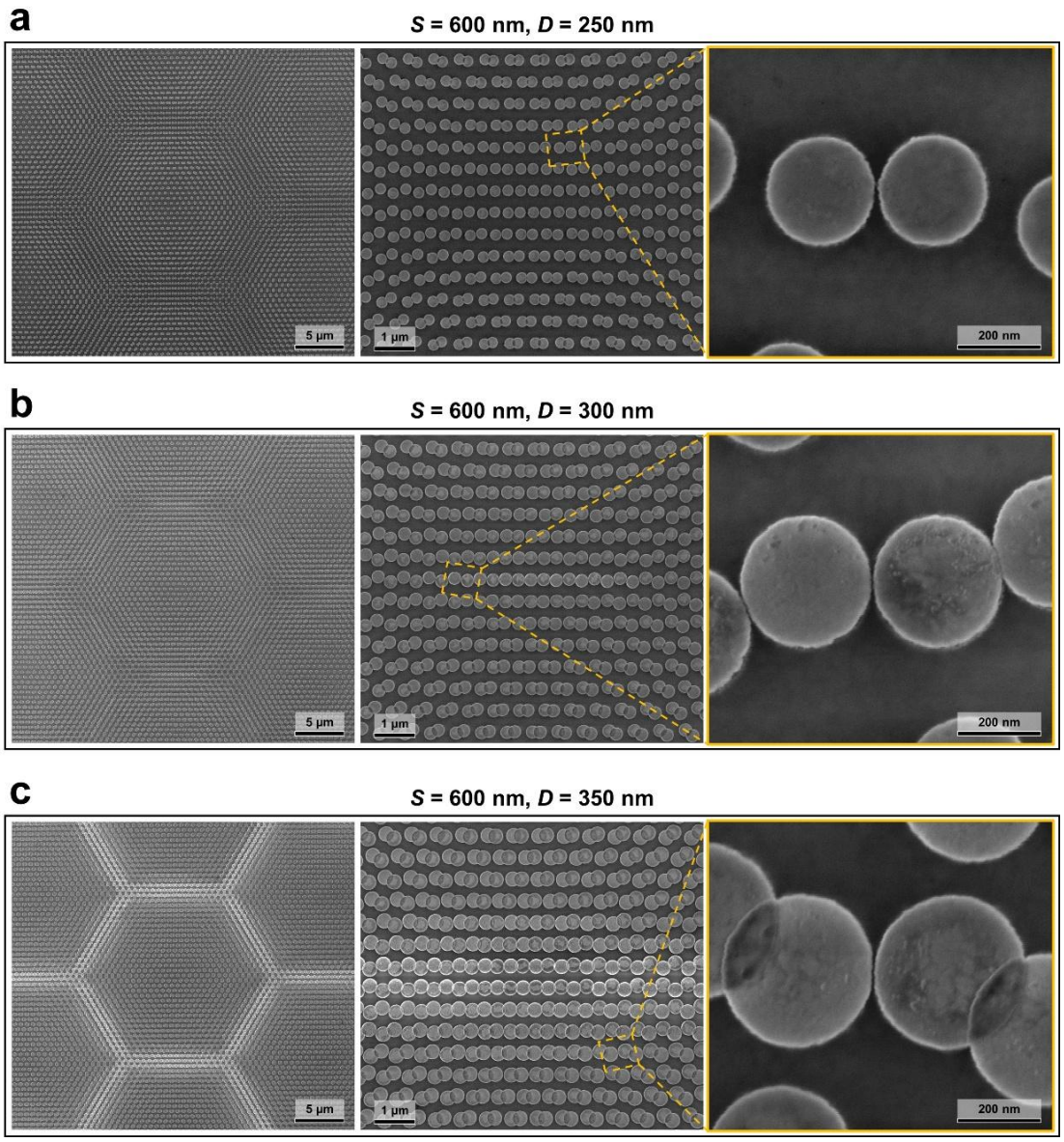

Figure 3.1 Experimental realization of plasmonic moiré superlattices with varying nanodisk diameters. SEM images of fabricated samples with three values of D: (a) 250, (b) 300, and (c) 350 nm, all fabricated with common parameters of S = 600 nm and $\alpha = 2°$. In each panel, the left image shows the superlattice primitive cells; the middle image shows a representative nanogap cluster region corresponding to the dashed-box areas in Figures 2.2a–c; and the right image shows one of the sub-10 nm gaps within the region.

3.2 Validation of the Two-Step Fabrication Approach

Considering the electron interaction volume in materials and the aspect ratio of developed electron-beam resist patterns, thin resist layers combined with low electron-beam currents are generally preferred for high-resolution patterning. However, thin resist layers inherently limit the maximum thickness of metal films that can be deposited without compromising the lift-off process. To alleviate this limitation, a previously reported two-step fabrication scheme [28–30] was adopted here. In this approach, relatively thick resist layers can be used, such as the 200-nm-thick resist employed in this work, thereby facilitating reliable lift-off processing while still enabling the formation of sub-10 nm nanogaps.

To assess the effectiveness of this fabrication scheme, a control sample was fabricated using a single-step approach, in which the entire moiré pattern was written in a single electron-beam exposure. In the control sample, only a negligible number of sub-10 nm gaps were observed. Figure 3.2 shows a plasmonic moiré superlattice sample in which the entire moiré pattern was defined in a single electron-beam exposure, with parameters S = 600 nm, D = 300 nm, and α = 2°. All other fabrication conditions were identical to those used for the corresponding two-step sample.

The SEM image of the nanogap cluster region in Figure 3.2b shows that many nanodisk pairs designed to form sub-10 nm gaps do not exhibit discernible separations. The smallest observed gap was approximately 10 nm, and such narrow gaps were less frequently observed than in the samples fabricated using the two-step method. Furthermore, as shown in the magnified image, the edges of nanodisks in the nanogap region are often accompanied by small metallic debris. These limitations result from the poor transfer of sub-10 nm features into the relatively thick (~200 nm) electron-beam resist layer. In contrast, the two-step process overcomes this issue [28–30] by eliminating the need for pattern transfer at such ultrasmall dimensions.

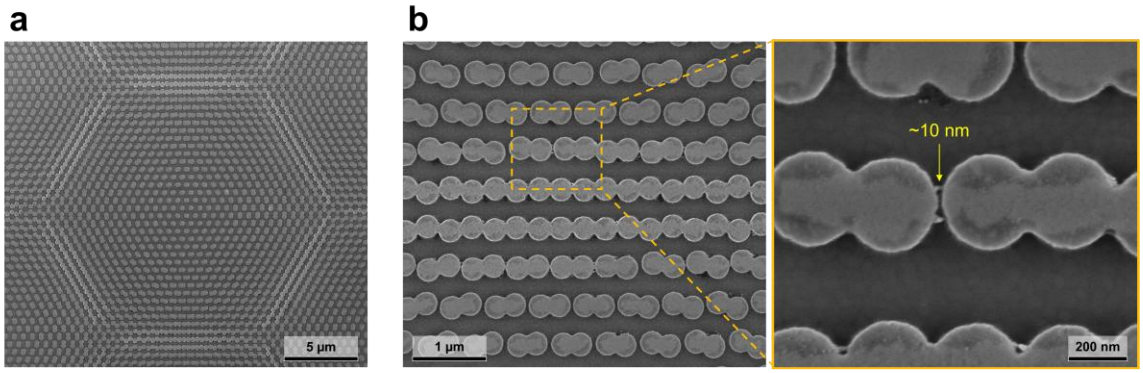

Figure 3.2 SEM images of a plasmonic moiré superlattice fabricated by a single-step process. (a) A representative primitive cell. (b) Nanogap cluster region in which sub-10 nm gaps are infrequently observed. The magnified view shows a nanogap approximately 10 nm wide, representing one of the smallest gaps observed in the sample.

3.3 Characterization of Nanogaps Using Voltage-Contrast SEM

While extremely narrow gaps may appear open in conventional SEM images, it is often difficult to determine whether the adjacent nanostructures are truly electrically isolated, as ultrathin metallic bridges or residues can lead to unintended electrical connections. Such connections can degrade performance in applications including optical field enhancement and quantum effects. For accurate characterization of the fabricated nanogaps, the voltage-contrast method was employed, which is effective in visualizing electrical isolation between small conducting features [48, 49]. In this method, distinct surface potentials between two closely spaced Au nanostructures were generated by introducing a pronounced difference in feature size and applying a 2 kV accelerating voltage to the primary electron beam.

As shown in Figure 3.3a, a substantial size difference between adjacent Au features was introduced using Au gratings composed of 30 nm Au on a 3 nm Ti adhesion layer, overlaid onto the moiré superlattice without controlled alignment. The grating was patterned to be electrically connected to a floating structure that is significantly larger than the primitive cell of the superlattice.

Figures 3.3b and 3.3c present voltage-contrast SEM images, in which electrically isolated Au nanodisks exhibit dark contrast due to suppressed secondary electron emission caused by positive charging [50]. In contrast, nanodisks connected to the large structure via the grating exhibit minimal charging owing to their substantially higher capacitance, resulting in bright contrast. The higher-magnification image in Figure 3.3b reveals that the nanodisks forming a sub-10 nm gap are electrically disconnected, as evidenced by the clear contrast. The gray-scale intensity profile along the dotted line further quantifies this contrast.

In comparison with Figure 3.3b, the nanodisks forming a sub-5 nm gap, as shown in the higher-magnification image in Figure 3.3c, exhibit slightly reduced contrast. The gray-scale intensity profile along the dotted line indicates that the nanodisk forming the sub-5 nm gap with the grating-connected nanodisk appears slightly brighter than the nanodisk on the right-hand side, which is evidently not connected to the grating. This contrast difference can be attributed either to electron transfer mediated by tunneling effects or to extremely narrow conductive pathways formed by edge roughness of the nanodisks. Further insight into the intermediate contrast may be obtained using higher-resolution and complementary imaging techniques, such as transmission electron microscopy (TEM) and conductive atomic force microscopy (C-AFM) [51], as well as by applying an external bias to enable controlled voltage-contrast measurements [52]. Overall, the voltage-contrast method demonstrates that the numerically predicted nanogaps can be experimentally realized, although gaps below approximately 5 nm could not be conclusively verified under the present experimental conditions.

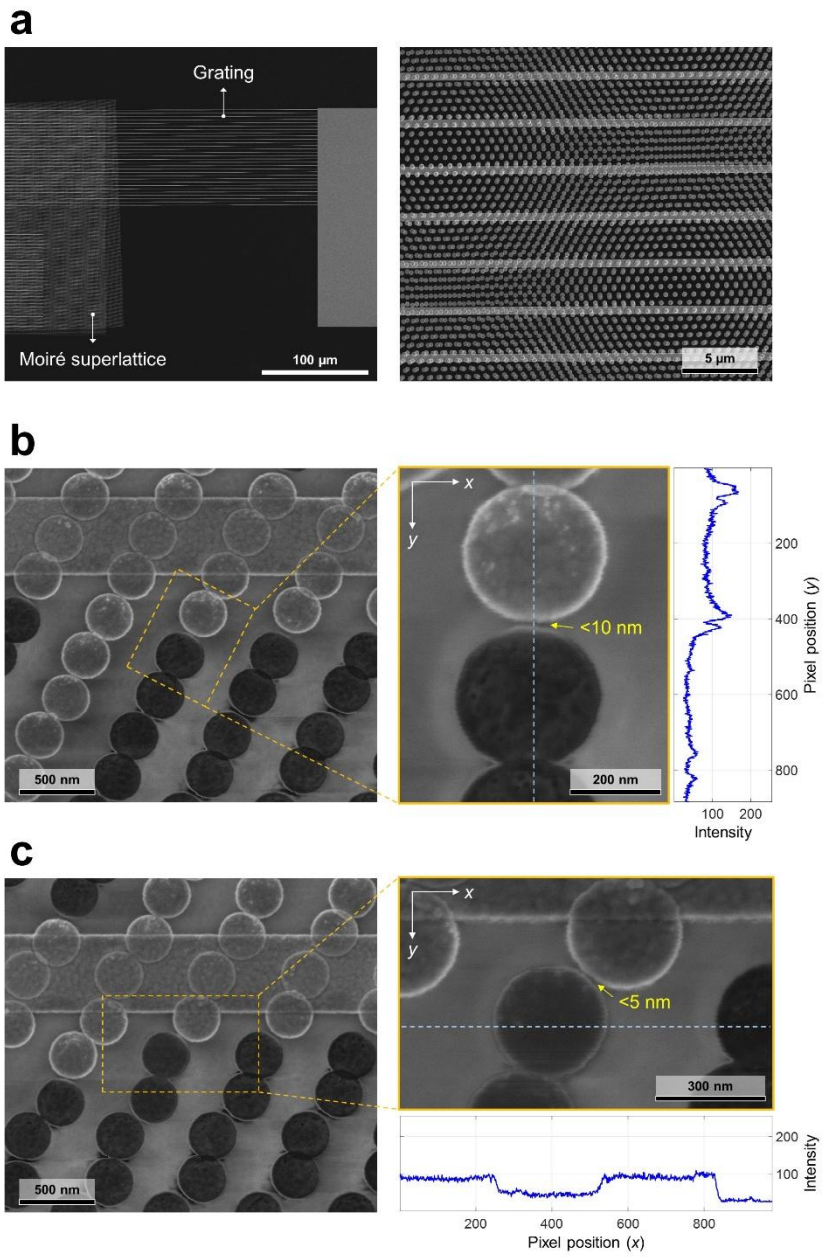

Figure 3.3 Experimental verification of electrical isolation in nanogaps using voltage-contrast SEM. (a) SEM images of an Au grating structure superimposed on the moiré superlattice (S = 600 nm, D = 300 nm, α = 2°), designed to enable voltage-contrast measurements. The Au grating electrically connects randomly selected nanodisks to a significantly larger feature (partially shown in the left image). (b, c) Voltage-contrast SEM images showing contrast variations among nanodisks depending on their electrical

connectivity to the grating. In the higher-magnification images, gray-scale intensity profiles along the dotted lines quantitatively represent the relative voltages induced in the nanodisks. The measured nanogap widths are <10 nm in (b) and <5 nm in (c). Electron-beam accelerating voltages of 5 kV and 2 kV were used for (a) conventional SEM imaging and (b, c) voltage-contrast SEM imaging, respectively.

3.4 Electromagnetic Simulation of Nanogap Field Enhancement

Full-wave electromagnetic simulations were performed using the finite-element method implemented in COMSOL Multiphysics to evaluate the plasmonic field enhancement in the nanogap cluster region. To simplify the analysis, a periodic nanodisk array was modeled to examine the local optical response at the cluster center, as indicated by the dotted circle in Figure 3.4a. In this region, the nanodisks exhibit a nearly periodic arrangement with minimal overlap. The chosen superlattice parameters were $S = 600$ nm, $D = 290$ nm, and $\alpha = 2°$, which yield nanogaps of approximately 10 nm at the center of the circular region.

Figure 3.4b illustrates the unit cell used in the simulation, with dimensions of 600 nm (S) along the x-direction and $\left(S\sqrt{3}\right)/2$ along the y-direction. The Au nanodisks have a diameter of 290 nm (D) and a thickness of 30 nm, with a center-to-center spacing of 300 nm, resulting in a nanogap width of 10 nm. The refractive indices of alumina (Al_2O_3) and Au at a wavelength of 633 nm were obtained experimentally by spectroscopic ellipsometry. Perfectly matched layers (PMLs) with a thickness of 800 nm were applied to the top and bottom of the unit cell. The incident illumination is modeled as a monochromatic plane wave at a wavelength of 633 nm, linearly polarized along the x-direction and propagating in the negative z-direction. Periodic boundary conditions are applied along the x- and y-directions. The computational domain was discretized using the “Extremely Fine” mesh setting, with the maximum and minimum mesh element sizes adjusted to 40 nm and 0.1 nm, respectively. To monitor the field magnitude, a point probe was positioned at the nanogap center, which corresponds to the midpoint between the two nanodisk centers, to record the electric field magnitude.

Figure 3.4c shows the normalized electric field magnitude at the nanogap center as a function of the dielectric spacer thickness, ranging from 10 to 500 nm in steps of 5 nm. The plot reveals distinct peaks of enhanced field magnitude, arising from different resonance coupling mechanisms. Notably, the strongest enhancement is observed at a spacer thickness of ~200 nm, primarily due to the near-field coupling of localized surface plasmons in the nanodisks.

These results demonstrate that appreciable field enhancement is readily attainable through tuning of the dielectric spacer thickness. Further enhancement can be realized by optimizing the overall superlattice structures for SERS applications, which will be discussed in the next chapter.

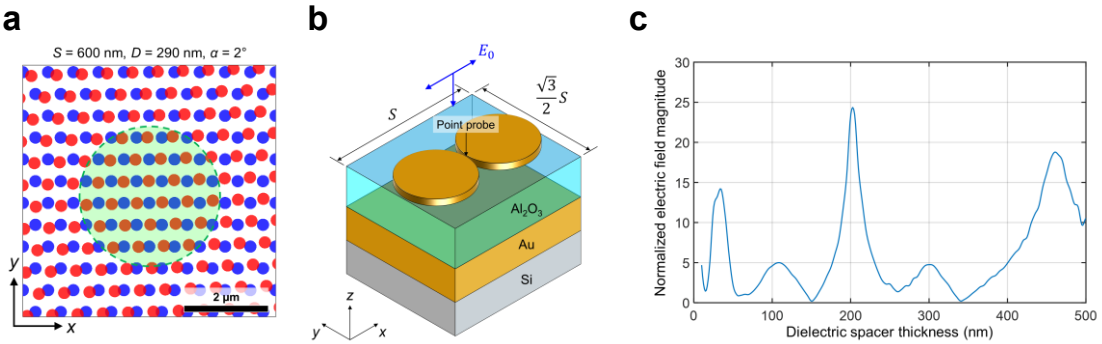

Figure 3.4 Numerical evaluation of plasmonic field enhancement in nanogap clusters and its dependence on dielectric spacer thickness. (a) Spatial distribution of nanodisks in the nanogap cluster region of the moiré superlattice with parameters S = 600 nm, D = 290 nm, and $\alpha = 2°$. A nearly periodic arrangement of nanodisks is apparent in the region marked by the dotted circle, which corresponds to the center of the nanogap cluster. (b) Schematic illustration of the unit cell structure and materials for simulating the optical response of the highlighted circular region shown in (a). (c) Plot of the normalized electric field magnitude at the nanogap center as a function of dielectric spacer thickness (10–500 nm), calculated at an excitation wavelength of 633 nm.

Chapter 4

ELEVATED PLASMONIC MOIRÉ SUPERLATTICES FOR SURFACE-ENHANCED RAMAN SPECTROSCOPY

This chapter is based on:

C. Hwang and A. Scherer, "Plasmonic Moiré Superlattices for Robust Nanogap Cluster Formation," *Small Methods* 10, no. 6 (2026): e02269. DOI: 10.1002/smtd.202502269

This chapter extends the proposed approach to elevated plasmonic moiré structures and verifies their performance for SERS applications.

4.1 Fabrication of Elevated Plasmonic Moiré Superlattices

The presented moiré structures serve as a fundamental structural framework that can be further refined and optimized for specific applications. To explore the practical relevance of this approach, its applicability to SERS, a representative sensing technique that critically relies on the field-enhancing capability of plasmonic structures, is demonstrated. Beyond strong field enhancement, a large area of electromagnetic hotspots accessible to target analyte molecules is another essential factor for achieving high sensitivity in SERS applications. Elevated plasmonic nanogap array structures have therefore been explored to provide larger accessible field-enhancing areas [53–55], thereby mitigating substrate effects [56]. Such structures typically rely on controlled material deposition processes, enabling relatively precise control over nanogap dimensions through the gradual narrowing of gaps in pre-defined nanostructures. However, even with carefully controlled deposition, reliably realizing clusters of ultranarrow gaps in the presence of typical fabrication errors remains challenging. This challenge can be alleviated by leveraging the geometry-driven robust formation of nanogaps enabled by moiré configurations.

Figure 4.1 illustrates the fabrication process for elevated plasmonic moiré superlattices designed for SERS. First, SU-8 photoresist was spin-coated onto a Si substrate and hard-baked to form a cross-linked SU-8 layer. A 200-nm-thick PMMA resist layer was then spin-coated on the SU-8 layer, as shown in Figure 4.1a. Next, as illustrated in Figure 4.1b, two twisted periodic array patterns were sequentially exposed by EBL in the PMMA resist layer, followed by resist development. A 20-nm-thick Ti layer was then deposited by electron-beam evaporation, followed by metal lift-off, as illustrated in Figure 4.1c. The resulting patterned Ti layer served as an etch mask for the subsequent etching step. Figure 4.1d illustrates the step for realizing elevated structures via isotropic oxygen (O_2) plasma etching of the hard-baked SU-8 layer, resulting in Ti nanodisks supported on tapered SU-8 nanopillars. Finally, Ti and Au were deposited by sputter deposition to form elevated Au nanodisks with narrow gaps in the nanogap cluster regions, as illustrated in Figure 4.1e. The detailed fabrication process is as follows.

A hard-baked SU-8 polymer layer was fabricated on a single-side-polished Si substrate (12.5 × 12.5 cm^2). The SU-8 photoresist (SU-8 2000.5, Kayaku Advanced Materials) was spin-coated onto the substrate, followed by soft baking on a hot plate at 95 °C for 1 min. The coated layer was then exposed to ultraviolet light (405-nm wavelength, 25 $mW \cdot cm^{-2}$) for 10 s using a Karl Suss MA6/BA6 mask aligner (SUSS MicroTec SE) for sufficient cross-linking of the SU-8 layer. After exposure, the sample temperature was gradually increased to 190 °C and maintained for 5 min for hard baking. The SU-8 layer thickness was approximately 550 nm, as measured using a spectroscopic ellipsometer (M-2000, J.A. Woollam). A 200-nm-thick 950K PMMA layer was spin-coated onto the SU-8 polymer layer and baked at 180 °C for 4 min. The electron-beam writing of two twisted patterns of periodic hexagonal nanodisk arrays was sequentially performed without intermediate processing using an EBPG 5000+ system (Raith GmbH), with a beam current of 5 nA and an exposure dose of 600 $\mu C \cdot cm^{-2}$. The exposed PMMA was developed in a MIBK:IPA (1:3) solution for 60 s, followed by rinsing with IPA for 10 s and drying under a nitrogen flow. A 20-nm-thick Ti layer serving as an etch mask was deposited on the developed sample by electron-beam evaporation (ATC Orion, AJA International) at a deposition rate of 0.5 $Å \cdot s^{-1}$. We note that the Ti layer used as

the etch mask is not unique, and other materials compatible with oxygen plasma etching could also be employed without altering the underlying fabrication strategy. Metal lift-off was carried out in acetone, followed by rinsing with IPA and drying under nitrogen. Subsequently, isotropic oxygen plasma etching (100 W, 6 sccm, ~110 mTorr) of the hard-baked SU-8 layer was performed for 200 s with the patterned Ti etch mask using a plasma cleaner (Tergeo Plus Plasma Cleaner, PIE Scientific). The resulting etch depth of the non-patterned SU-8 layer was approximately 220 nm. As a final step, a Ti adhesion layer (10 nm, 3 mTorr, DC 150 W) and Au layers (3 mTorr, RF 100 W) with thicknesses of 80, 100, and 150 nm were deposited on three separate samples by magnetron sputtering (ATC Orion 8, AJA International), yielding three samples with different Au thicknesses.

The use of SU-8 for nanopillars enables a simple and broadly accessible fabrication process due to its straightforward deposition via spin coating. Moreover, isotropic O_2 plasma etching of hard-baked SU-8 can be performed using standard plasma cleaning equipment, in contrast to previously reported approaches that require more complex or specialized processing steps [53–55].

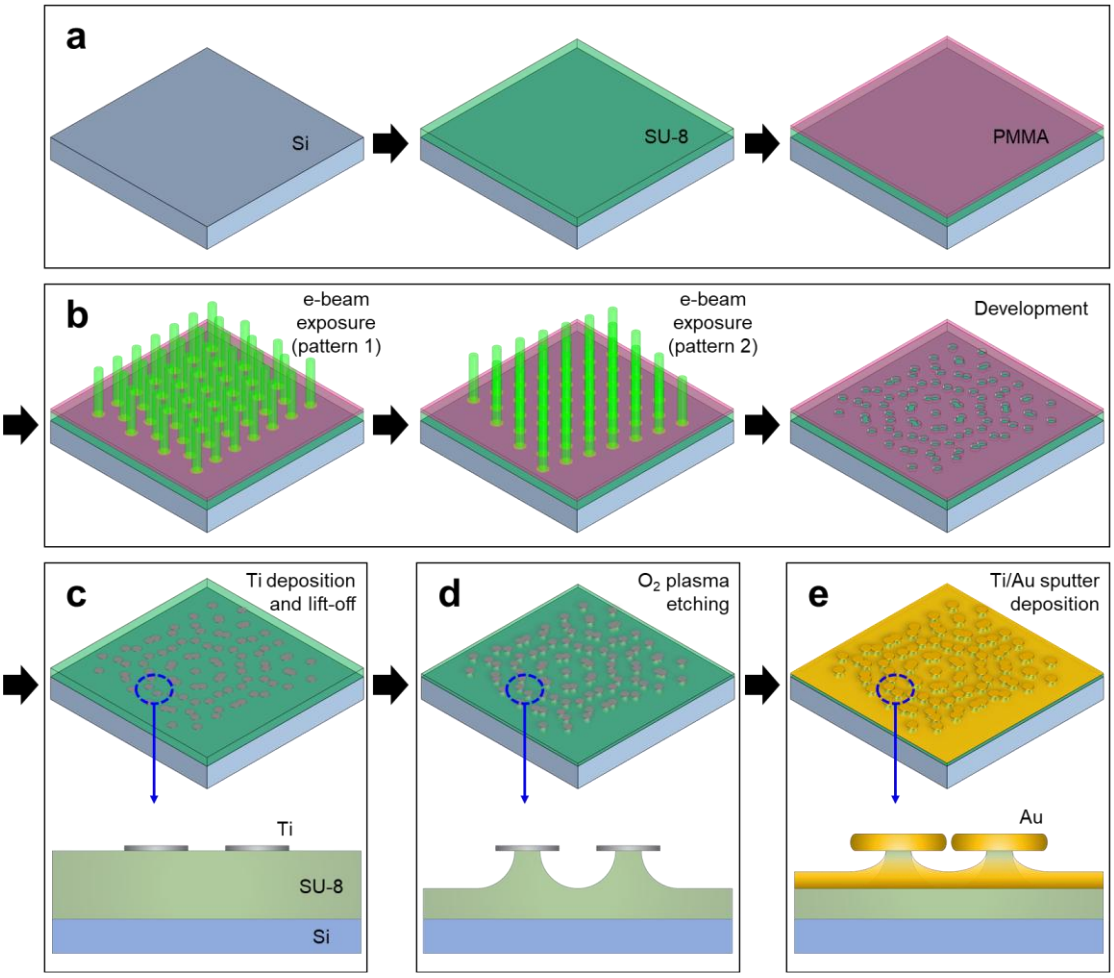

Figure 4.1 Schematic representation of the fabrication process for elevated plasmonic moiré superlattices. (a) Formation of a cross-linked SU-8 layer on a Si substrate by spin coating and hard baking, followed by spin coating of a 200-nm-thick PMMA resist layer. (b) EBL patterning of twisted periodic nanodisk arrays in the PMMA resist layer. (c) Formation of a patterned Ti etch mask by evaporation and lift-off. (d) Isotropic O_2 plasma etching to produce SU-8 nanopillars supporting Ti nanodisks. (e) Ti/Au sputter deposition to form elevated Au nanodisks with narrow gaps.

4.2 Design of Elevated Moiré Structures with Fabrication Considerations

In the moiré superlattice design for the elevated structures, the center-to-center spacing (S) and the twist angle (α) were set to 900 nm and 1°, respectively. The nanodisk diameter of the 20-nm-thick Ti etch mask was set to 370 nm, such that the resulting Au nanodisks had a diameter of approximately 450 nm (D) after sputter deposition of Ti and Au with thicknesses of 10 and 100 nm, respectively.

Figure 4.2 presents the calculated spatial distributions of nanodisks in Array 2 that form sub-10, sub-20, and sub-30 nm gaps with nanodisks in Array 1 for D = 430, 450, and 470 nm, with fixed parameters of S = 900 nm and α = 1°. For each nanogap-forming nanodisk, the average nanogap alignment angle (0–180°) is indicated by the color of the corresponding nanodisk. The results show that the rings of sub-10 nm gap formation, which mainly contribute to strong electromagnetic field enhancement, gradually expand and merge at D = 450 nm, and form crossings at D = 470 nm. These results indicate that strong field enhancement is expected at the midpoint between adjacent primitive cells when D is approximately 450 nm or slightly larger, due to the high density of sub-10 nm gaps.

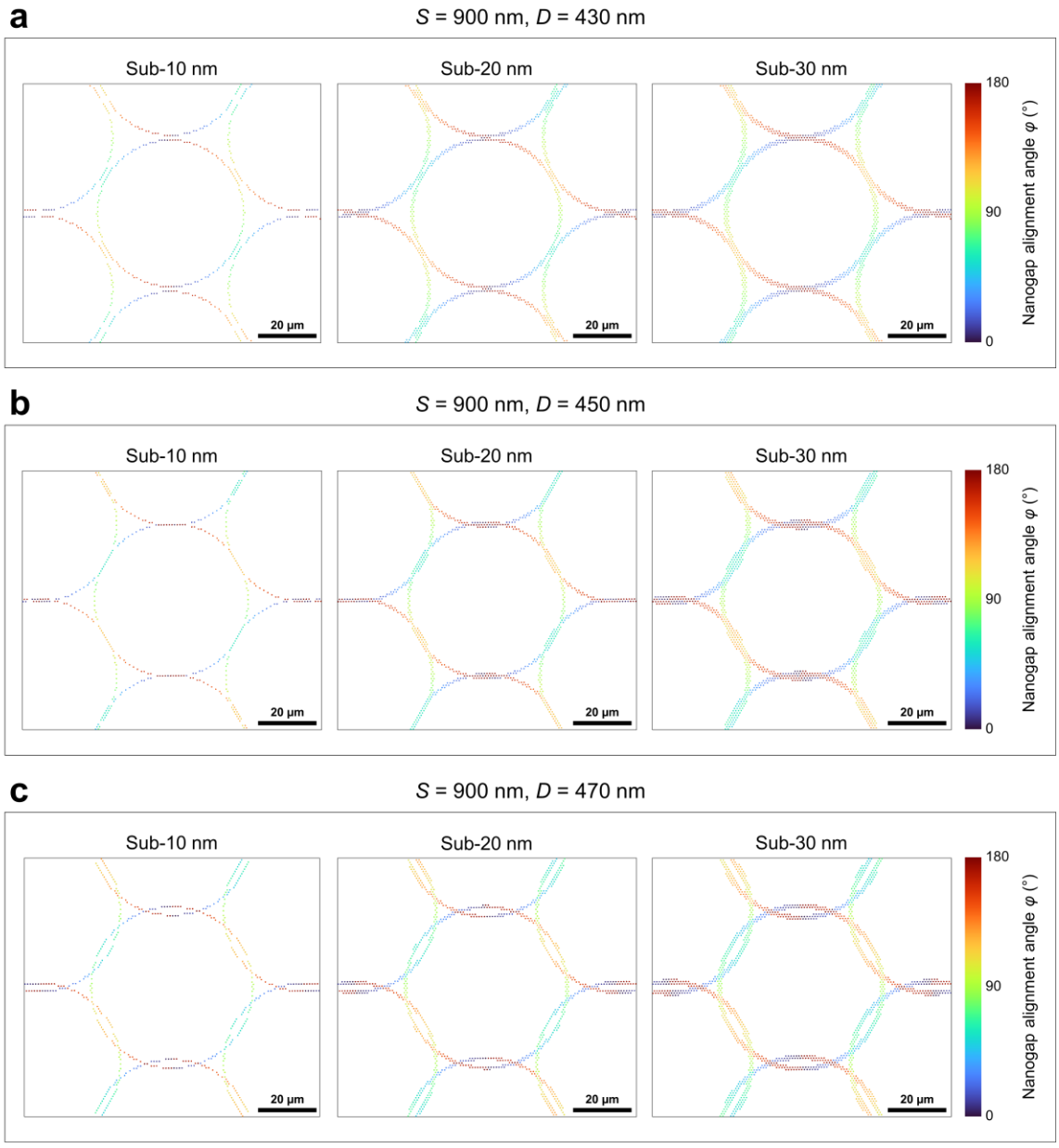

Figure 4.2 Numerical analysis of nanogap cluster formation and its dependence on nanodisk diameter in plasmonic moiré superlattices. Spatial distributions of nanodisks in Array 2 forming sub-10, sub-20, and sub-30 nm gaps with nanodisks in Array 1 for (a–c) D = 430, 450, and 470 nm, respectively, with fixed parameters of S = 900 nm and α = 1°. The color of each nanodisk represents the average nanogap alignment angle (0–180°). As D increases, the rings of sub-10 nm gap formation expand, merge, and eventually form crossings, indicating an increased density of strongly field-enhancing nanogaps.

4.3 SEM Characterization of Elevated Nanogap Structures

The fabricated structures were characterized by SEM (Figure 4.3). Figure 4.3a presents the structure obtained after O_2 plasma etching of the SU-8 layer, corresponding to the fabrication step illustrated in Figure 4.1d. The top-view image (left) shows the region around the interface between two adjacent primitive cells, revealing a quasi-periodic arrangement of 20-nm-thick Ti nanodisks with comparatively large separations between adjacent nanodisks. The tilted-view image (70° tilt, right) confirms that the Ti nanodisks are elevated and supported by tapered SU-8 nanopillars.

Figure 4.3b shows the Au nanodisks formed after sputter deposition of Ti and Au, corresponding to the fabrication step illustrated in Figure 4.1e. The top-view image (left) reveals a distribution of narrowed and well-aligned nanogaps, and the magnified image further highlights sub-10 nm gaps within the nanogap cluster regions. The side-view image (89° tilt, right) shows pillar-supported Au nanodisks with rounded sidewalls, consistent with the slightly conformal nature of the sputter deposition process. Such densely packed elevated nanodisks provide large accessible sensing areas for Raman signal enhancement.

Additionally, two more samples were fabricated by varying the Au sputter deposition thickness. Figure 4.4 shows the nanogap cluster regions of samples prepared with Au thicknesses of 80 and 150 nm, resulting in Au nanodisk diameters of approximately 430 and 470 nm, respectively. The magnified images on the right confirm that, despite the significant variation in fabrication conditions, extremely small nanogaps were consistently obtained.

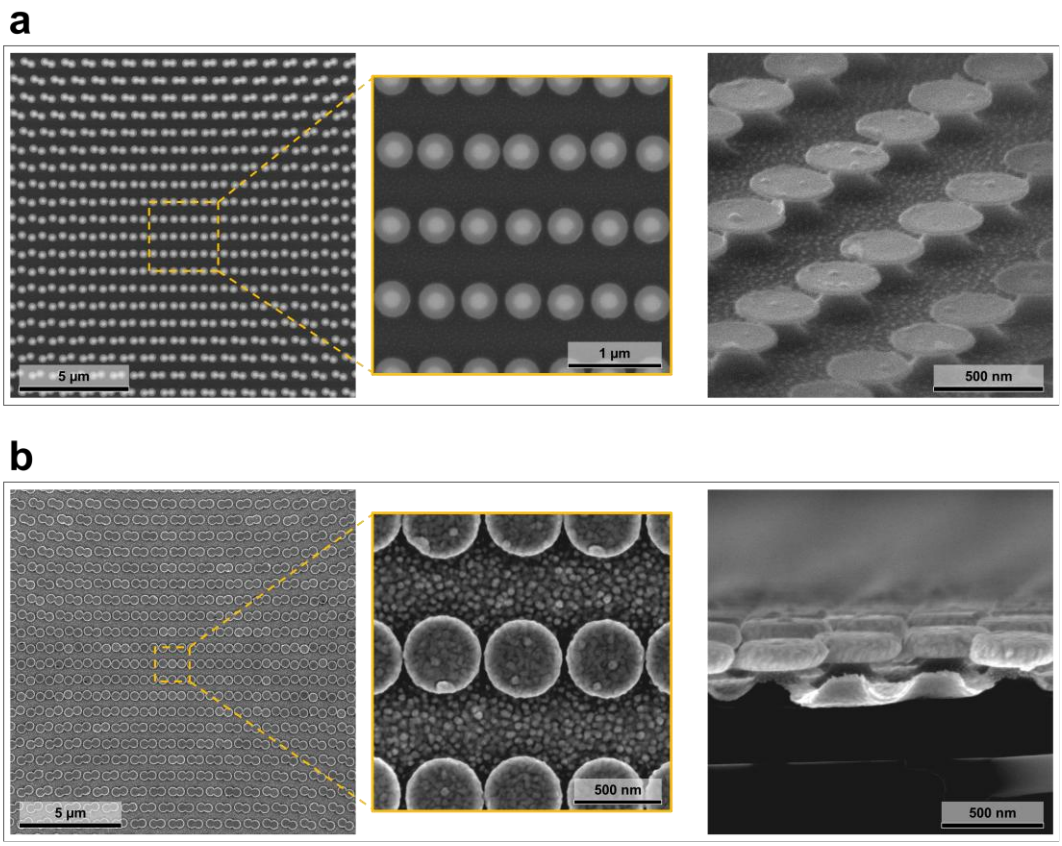

Figure 4.3 SEM characterization of elevated plasmonic moiré superlattices at different stages of the fabrication process. Elevated plasmonic moiré superlattice structures before (a) and after (b) sputter deposition of Ti (10 nm) and Au (100 nm). (a) Top-view (left) and 70° tilted view (right) images of quasi-periodically arranged Ti nanodisks supported by SU-8 nanopillars (step shown in Figure 4.1d). (b) Top-view (left) and 89° tilted view (right) images of pillar-supported Au nanodisks with well-aligned narrow nanogaps formed after Ti/Au sputter deposition (step shown in Figure 4.1e).

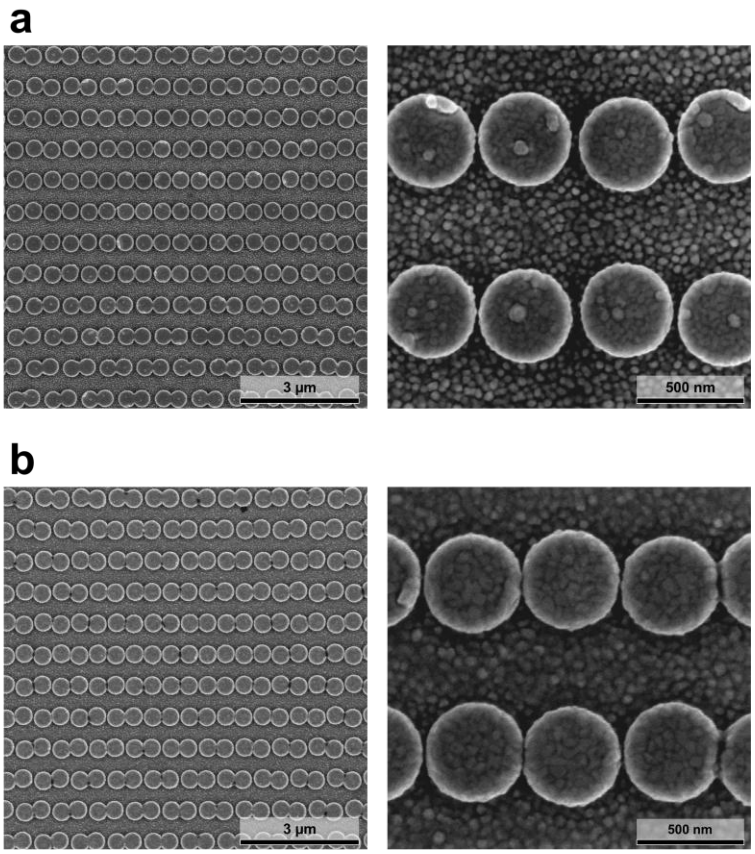

Figure 4.4 SEM characterization of nanogap clusters formed in elevated plasmonic moiré superlattices with varying Au thickness. SEM images of nanodisks in elevated plasmonic moiré superlattices with (a) 80- and (b) 150-nm Au sputter deposition. The measured nanodisk diameters are approximately 430 nm for (a) and 470 nm for (b).

4.4 Electromagnetic Simulation of Elevated Nanogap Structures

Based on the experimentally observed structure, full-wave electromagnetic simulations were performed using COMSOL Multiphysics to investigate the electric field magnitude distribution in the nanogap cluster region, assuming a periodic arrangement of nanodisks within the region. The simulations were carried out using the same superlattice design parameters as those employed in the experiments (S = 900 nm, D = 450 nm, and α = 1°), which yield quasi-periodic nanogap arrangements within the nanogap cluster regions (Figure 4.5a).

The simulated structure was based on the SEM observations shown in Figure 4.3b, with minor structural simplifications for numerical modeling. Figure 4.5b illustrates the unit-cell geometry projected onto three orthogonal planes for the simulations. The dimensions along the *x*- and *y*-directions are 450 nm ($S/2$) and 779 nm ($S\sqrt{3}/2$), respectively. The edge-rounded Au nanodisks were modeled with a diameter of 440 nm (*D*) and a thickness of 100 nm. Each Au nanodisk was positioned on a 20-nm-thick Ti nanodisk, which corresponds to the etch mask used in the experimental implementation. The refractive indices of Au, Ti, SU-8, and Si were obtained from the COMSOL Material Library.

PMLs with a thickness of 400 nm were applied to the top (air) and bottom (Si substrate) boundaries of the unit cell. The incident illumination was modeled as a monochromatic plane wave with a wavelength of 633 nm, linearly polarized along the *x*-direction and propagating in the negative *z*-direction. Periodic boundary conditions were applied along the *x*- and *y*-directions. A periodicity of 450 nm along the *x*-direction corresponds to a nanogap width of approximately 10 nm. The computational domain was discretized using the "Extremely Fine" mesh setting, with the maximum and minimum mesh element sizes set to 24 nm and 0.1 nm, respectively.

Figure 4.5c shows the electric field magnitude profile in a cross-sectional plane through the Au nanodisk. The field magnitude was normalized to the magnitude of the incident electric field. The simulated field distribution indicates that strongly enhanced optical hotspots are generated within the nanogap regions. Considering that the SERS enhancement factor is approximately proportional to the fourth power of the local electric field enhancement, the simulated results exhibit good agreement with the experimentally measured SERS enhancement factors.

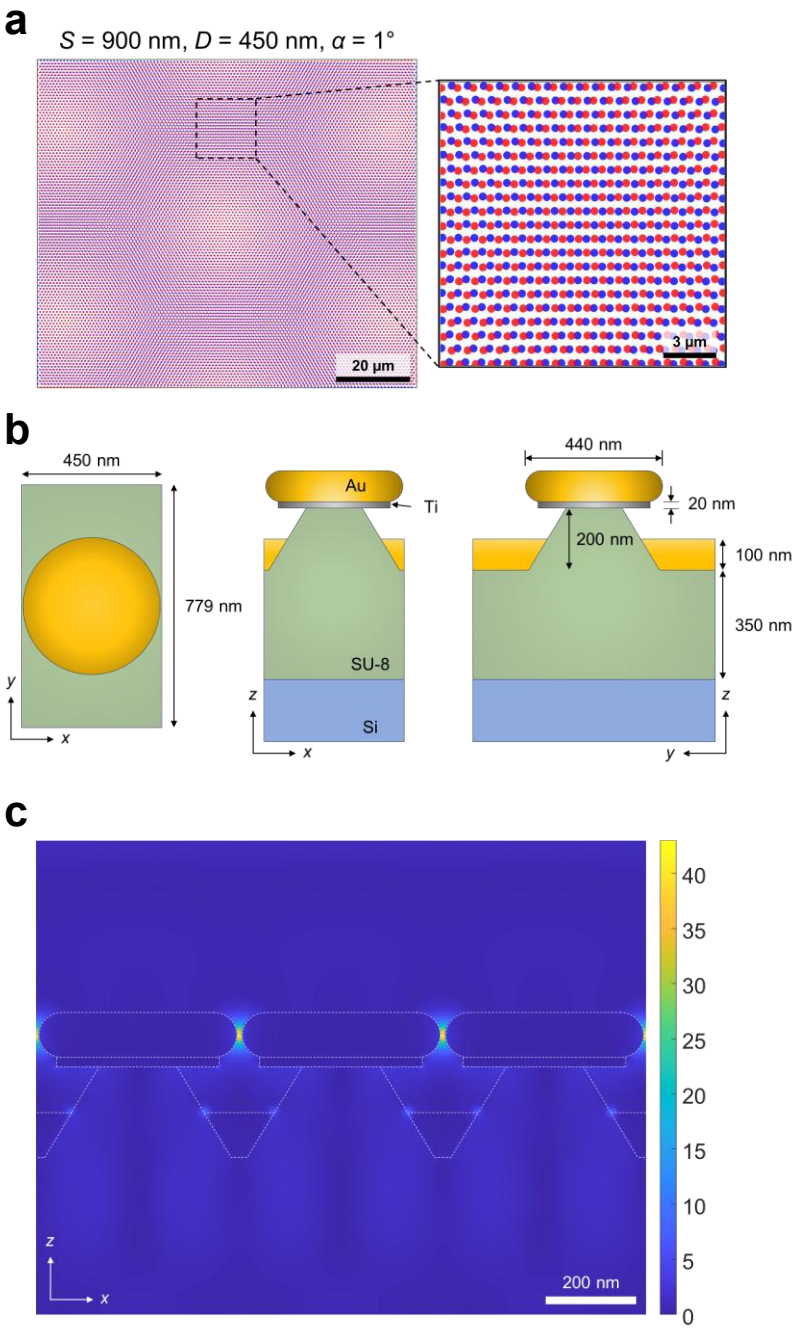

Figure 4.5 Full-wave electromagnetic simulation of electric field enhancement in elevated plasmonic nanogap clusters. (a) Numerically calculated distribution of nanodisks in a moiré superlattice (S = 900 nm, D = 450 nm, and α = 1°), showing a quasi-periodic arrangement within a nanogap cluster region. (b) Unit-cell geometry projected onto three orthogonal planes used in the simulations. (c) Normalized electric field magnitude

distribution in an *x*–*z* cross-sectional plane through the Au nanodisk, showing strongly enhanced optical hotspots localized within the nanogap regions.

4.5 SERS Performance of Elevated Moiré Superlattices

The field-enhancement performance of the fabricated elevated plasmonic moiré superlattices was evaluated by Raman measurements with 4-mercaptobenzoic acid (4-MBA), selected due to its stable adsorption on Au surfaces and well-defined Raman response. A self-assembled monolayer (SAM) of 4-MBA molecules was formed on the Au surface [57] by immersing the samples in a 0.1 mM ethanolic solution of 4-MBA for approximately 24 h, followed by thorough rinsing with ethanol to remove non-adsorbed molecules. Backscattered Raman signals from the SAM-functionalized samples were collected using a Renishaw inVia confocal Raman microscope (633 nm excitation, 50× objective, an 1800 lines·mm^{-1} grating, NA = 0.75). Instrument control and data post-processing were carried out using the manufacturer-provided software (WiRE). The excitation laser power was set to 1%, corresponding to an incident power of approximately 40 μW at the sample plane. The acquisition time for each spectrum was 5 s. SERS mapping images were generated using the "Dynamic Mapping" function in the WiRE software. Each acquired spectrum was smoothed using Savitzky–Golay filtering (window size = 9, polynomial order = 3) and subsequently baseline-subtracted using the intelligent fitting mode (polynomial order = 11, noise tolerance = 1.5).

Figure 4.6a shows Raman intensity maps of the nanogap cluster regions for three samples with different Au deposition thicknesses of 80, 100, and 150 nm. The integrated intensity of the Raman peak at 1588 cm^{-1}, which is one of the two prominent Raman peaks of 4-MBA, was mapped over an area of 41 × 41 μm^2 with a step size of 1 μm. The incident light polarization was aligned along the *x*-direction, consistent with the predominant orientation of the nanogaps near the center of the mapped region. The measured intensity maps show that enhanced Raman signals are generated in the ring-shaped nanogap cluster regions. Moreover, these hotspot rings exhibit slightly different sizes due to variations in the nanodisk

sizes induced by the different Au deposition thicknesses. This trend is consistent with the numerical investigations of nanogap distributions for different nanodisk sizes.

Figure 4.6b presents representative Raman spectra obtained from the three samples. For comparison, the Raman spectrum of bulk 4-MBA is also included, with its intensity multiplied by a factor of 5 to improve peak visibility. The bulk 4-MBA reference sample was prepared by pressing a sufficient amount of 4-MBA powder onto a flat Au reflector substrate (100-nm-thick Au deposited on a Si substrate). Strongly enhanced Raman signals were observed from the nanogap cluster regions across all three samples, demonstrating the reliable formation of the moiré-based nanogaps despite fabrication variations. The measured enhancement factor increases with increasing Au thickness. This trend can be attributed to the enlargement of the nanogap cluster regions, which causes neighboring clusters to overlap as the nanodisk radius increases. Thicker Au deposition also results in an increased nanodisk sidewall area, thereby providing a larger accessible surface for analyte adsorption and contributing to the enhanced SERS response. Additionally, the slightly different SU-8 etching depths and Au deposition thicknesses among the three samples may have led to variations in hotspot intensity. This can be attributed to the fact that the field intensity in the nanogap is affected by changes in the Fabry–Pérot cavity resonance condition, which is coupled with nanogap-based hotspot generation in the nanogap cluster regions.

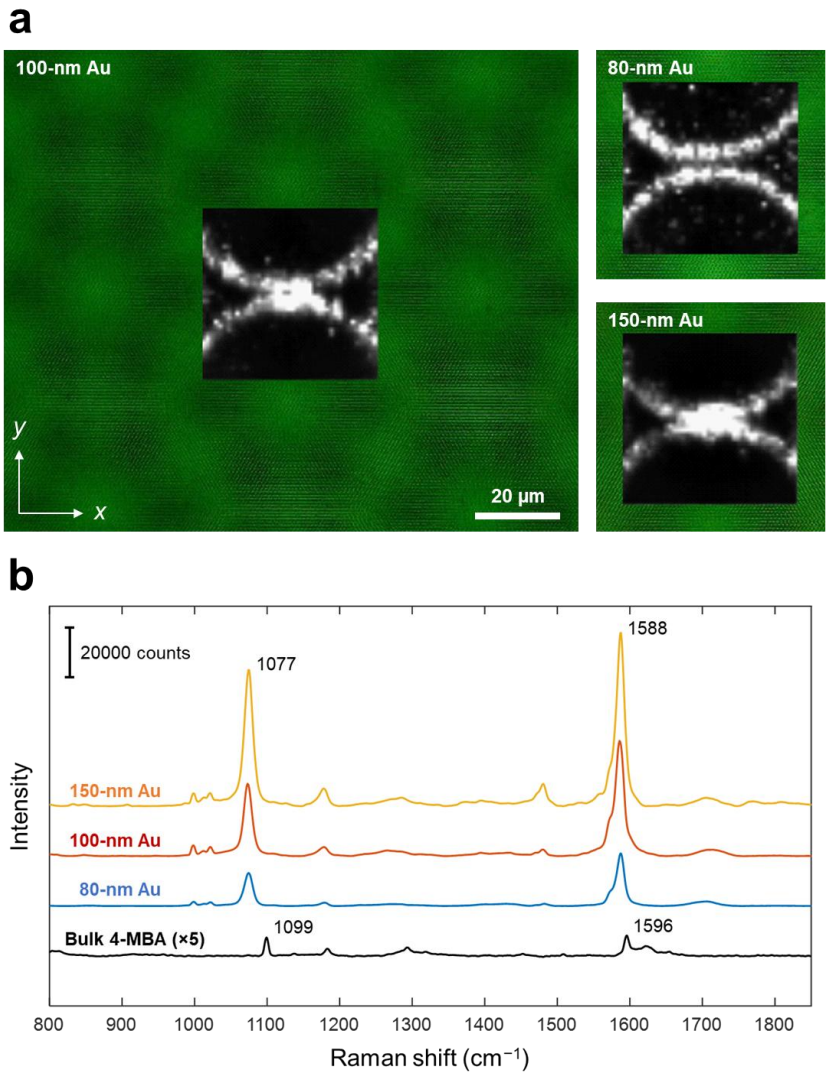

Figure 4.6 Experimental demonstration of SERS performance in elevated plasmonic moiré superlattices through Raman mapping and spectroscopy. (a) Raman intensity maps of the nanogap cluster regions for samples with Au deposition thicknesses of 80, 100, and 150 nm, obtained by mapping the integrated intensity of the 1588 cm^{-1} Raman peak. The maps reveal ring-shaped nanogap cluster regions exhibiting strong signal enhancement, with sizes that vary slightly with Au thickness. (b) Representative Raman spectra measured from the nanogap cluster regions of the three samples. The Raman spectrum of bulk 4-MBA is included for comparison and scaled by a factor of 5 for clarity. Raman spectra are vertically offset to aid visualization.

4.6 Polarization Dependence of SERS Enhancement

In general, the field enhancement in plasmonic structures depends on the polarization of the incident light. Based on the calculated nanogap alignment angles shown in Figure 4.2, nanogaps in the nanogap cluster region are expected to exhibit different levels of enhancement depending on their alignment relative to the incident polarization. To examine this effect, Raman intensity mapping was performed in the region where three primitive cells meet, as shown in Figure 4.7. The map clearly shows a dependence on the incident polarization due to variations in nanogap alignment along the nanogap cluster ring. In particular, the region indicated by the arrow exhibits minimal enhancement because the corresponding nanogaps are nearly orthogonal to the incident polarization aligned along the *x*-direction.

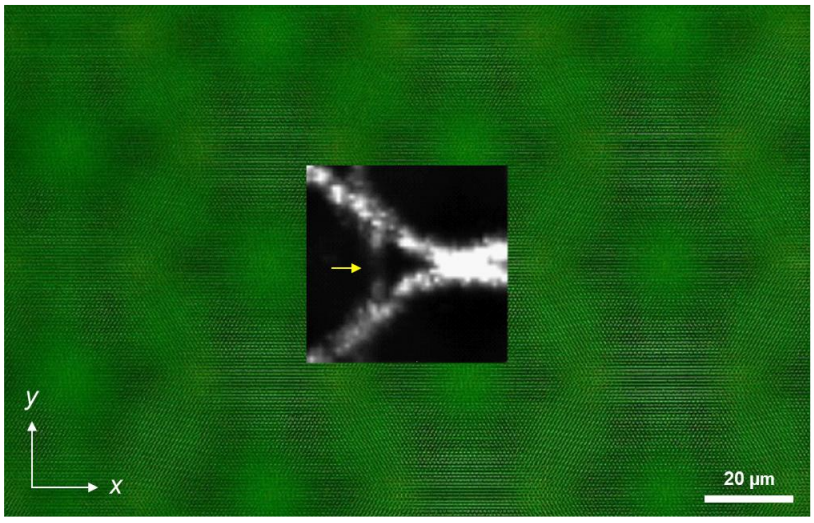

Figure 4.7 Raman intensity map showing polarization-dependent field-enhancement behavior of nanogaps in elevated plasmonic moiré superlattices. Intensity mapping (1588 cm^{-1}) over a 45 × 45 μm^2 (45 × 45 points) area around the point where three primitive cells meet was performed for the sample with 150-nm Au deposition. The Raman-scattered light from the nanogaps indicated by the arrow exhibits minimal intensity due to their near-orthogonal orientation with respect to the incident light polarization, which was linearly polarized along the *x*-direction.

4.7 Estimation of SERS Enhancement Based on Experimental Measurements

The enhancement factor (*EF*) for the 100-nm Au sample can be calculated using the following equation [57],

$$EF = \frac{I_{SERS} N_{bulk}}{I_{bulk} N_{SERS}},$$

where I_{SERS} and I_{bulk} are the integrated intensities of a characteristic Raman peak obtained from the SERS and bulk samples, respectively, and N_{SERS} and N_{bulk} represent the corresponding numbers of probe molecules contributing to the measured Raman signals.

Enhancement factors for the 4-MBA monolayer-coated elevated plasmonic moiré superlattice samples were calculated using the integrated intensities of the 1588 cm^{-1} peak for the SERS samples and the 1596 cm^{-1} peak for the bulk sample. For the sample with a 100 nm Au sputter-deposited layer, the measured intensity ratio was $I_{SERS}/I_{bulk} = 28.12$ (Figure 4.6b).

The laser spot area and focal depth were taken to be 2 μm^2 and 20 μm, respectively, yielding an estimated detection volume of 40 μm^3 for the bulk 4-MBA measurement. Using a bulk density of 1.5 $g \cdot cm^{-3}$ and a molecular weight of 154.19 $g \cdot mol^{-1}$ for 4-MBA, the number of molecules contributing to the Raman signal was estimated to be $N_{bulk} = 2.34 \times 10^{11}$. For the SERS measurement, a molecular footprint of 0.75 nm^2 per 4-MBA molecule was assumed, and the effective Au surface area of the SERS substrate was approximated to be identical to that of a flat Au surface. Based on these assumptions, the number of molecules contributing to the SERS signal was estimated to be $N_{SERS} = 2.67 \times 10^6$. Using these values, the SERS enhancement factor was calculated to be approximately $EF = 2.46 \times 10^6$.

Chapter 5

CONCLUSIONS

This chapter is based on:

C. Hwang and A. Scherer, "Plasmonic Moiré Superlattices for Robust Nanogap Cluster Formation," *Small Methods* 10, no. 6 (2026): e02269. DOI: 10.1002/smtd.202502269

This thesis demonstrates plasmonic moiré superlattices that enable the geometry-driven formation of nanogap clusters. Unlike conventional approaches limited by lithographic resolution, this strategy exploits the intrinsic geometry of moiré configurations. Numerical and experimental investigations confirm that simple stacking of two twisted nanodisk arrays on a planar substrate can generate dense nanogap clusters even in the presence of typical patterning imperfections. The formation of ultranarrow gaps is verified using voltage-contrast SEM, providing direct evidence of electrical isolation across the nanogaps beyond conventional morphological imaging. Furthermore, elevated plasmonic moiré superlattices are introduced, and their practical relevance is demonstrated through surface-enhanced Raman spectroscopy, showing consistently high sensitivity across different fabrication conditions.

Although EBL was employed for proof-of-concept demonstrations, the approach is inherently scalable and compatible with standard large-area lithographic techniques, including deep ultraviolet lithography and laser interference lithography. This advantage, together with the robust formation of extremely small nanogaps, enables cost-effective implementation for real-world applications.

Further investigations are warranted to better understand and validate nanogap formation and characterization. In the present study, intermediate voltage contrast was observed in voltage-contrast SEM measurements, which limited the reliable verification of sub-5 nm nanogaps.

This issue may be mitigated by fabricating samples with smaller geometric parameters, where reduced nanodisk radii could suppress unintended electrical contact arising from edge roughness during fabrication. Additionally, a slight reduction of the Au thickness below 30 nm may further help minimize such effects.

Alternative experimental approaches may also be explored. The use of different plasmonic metals and variation of SEM acceleration voltages could provide further insight into voltage contrast behavior. For more precise characterization of nanogap widths, higher-resolution imaging techniques such as transmission electron microscopy (TEM) can be employed. This approach would require the fabrication of plasmonic moiré superlattices on electron-transparent substrates, such as silicon nitride membranes with thicknesses below 100 nm.

Moreover, the voltage-contrast SEM methodology itself can be further developed. In this thesis, randomly selected nanodisks were connected to relatively large Au floating structures to enable voltage-contrast imaging. A more advanced approach would involve applying an external bias to the Au structure and measuring the steady-state contrast while sweeping the voltage could provide a more systematic approach. Such studies may offer deeper insight into tunneling phenomena across nanogaps, as well as their characterization using voltage-contrast SEM.

While the present study primarily focuses on nanogap-induced near-field enhancement, which is directly relevant to applications such as SERS, dark-field measurements could offer additional information on the far-field optical response of the system. In particular, dark-field microscopy imaging and spectroscopy could be employed to probe spatial variations in far-field plasmonic resonances across the structure, including differences between nanogap-rich hotspot clusters and non-overlapping regions. Such complementary characterization may help establish a more comprehensive understanding of the relationship between near-field hotspot formation and far-field plasmonic behavior in moiré superlattices.

Beyond these characterization approaches, the proposed structure can be further developed to incorporate additional functionalities. For example, polydimethylsiloxane (PDMS), a biocompatible and mechanically flexible material, has been widely utilized for precise control of nanoscale gaps through adjustable deformation [58]. Such a material system can be readily incorporated into the moiré superlattice architecture proposed in this thesis. Specifically, elevated moiré superlattices could be fabricated on a PDMS substrate, where thermal or mechanical modulation of the PDMS layer would enable controlled variation of the overall lattice dimensions, thereby allowing fine tuning of the nanogap widths. This type of dynamically tunable structure may enable the development of adaptable SERS substrates, where the nanogap geometry can be optimized according to the properties of target analyte molecules.

Another possible approach to further enhance the performance of the proposed structure is the application of a reflow process to reduce plasmonic losses and thereby improve field enhancement. In multi-grained Au nanodisks, a relatively large grain boundary area can lead to increased plasmonic losses and reduced field enhancement. By applying a reflow process [59], individual nanodisks may be effectively welded and transformed toward a single-crystal-like structure, which can reduce such losses and enhance electromagnetic field confinement within nanogaps. However, implementation of this approach requires careful consideration of material stability, as Au reflow typically requires temperatures exceeding 500 °C. Therefore, the supporting structure must be composed of materials that can withstand such thermal conditions without deformation.

Overall, this thesis establishes a scalable, geometry-driven framework for nanogap structures that overcomes conventional lithographic limitations. This framework provides a broadly accessible platform for future studies of nanogap-mediated phenomena in quantum optics and advanced sensing applications [60–63].

BIBLIOGRAPHY

1. H. Altug, S.-H. Oh, S. A. Maier, and J. Homola, "Advances and Applications of Nanophotonic Biosensors," *Nat. Nanotechnol.* 17 (2022): 5. DOI: 10.1038/s41565-021-01045-5
2. M. E. Stewart, C. R. Anderton, L. B. Thompson, *et al.*, "Nanostructured Plasmonic Sensors," *Chem. Rev.* 108, no. 2 (2008): 494. DOI: 10.1021/cr068126n
3. J. N. Anker, W. P. Hall, O. Lyandres, N. C. Shah, J. Zhao, and R. P. Van Duyne, "Biosensing with Plasmonic Nanosensors," *Nat. Mater.* 7 (2008): 442. DOI: 10.1038/nmat2162
4. S. Roy and Z. Gao, "Nanostructure-Based Electrical Biosensors," *Nano Today* 4, no. 4 (2009): 318. DOI: 10.1016/j.nantod.2009.06.003
5. J. R. Ferraro, K. Nakamoto, C. W. Brown, *Introductory Raman Spectroscopy*, Academic Press, San Diego, CA 1994.
6. K. Kneipp, Y. Wang, H. Kneipp, *et al.*, "Single Molecule Detection Using Surface-Enhanced Raman Scattering (SERS)," *Phys. Rev. Lett.* 78, no. 9 (1997): 1667. DOI: 10.1103/PhysRevLett.78.1667
7. S. Nie and S. R. Emory, "Probing Single Molecules and Single Nanoparticles by Surface-Enhanced Raman Scattering," *Science* 275, no. 5303 (1997): 1102. DOI: 10.1126/science.275.5303.1102
8. P. L. Stiles, J. A. Dieringer, N. C. Shah, and R. P. Van Duyne, "Surface-Enhanced Raman Spectroscopy," *Annu. Rev. Anal. Chem.* 1 (2008): 601. DOI: 10.1146/annurev.anchem.1.031207.112814
9. X. Wang, S.-C. Huang, S. Hu, S. Yan, and B. Ren, "Fundamental Understanding and Applications of Plasmon-Enhanced Raman Spectroscopy," *Nat. Rev. Phys.* 2 (2020): 253. DOI: 10.1038/s42254-020-0171-y
10. C. E. Talley, J. B. Jackson, C. Oubre, *et al.*, "Surface-Enhanced Raman Scattering from Individual Au Nanoparticles and Nanoparticle Dimer Substrates," *Nano Lett.* 5, no. 8 (2005): 1569. DOI: 10.1021/nl050928v
11. P. Alonso-González, P. Albella, M. Schnell, J. Chen, F. Huth, A. García-Etxarri, *et al.*, "Resolving the Electromagnetic Mechanism of Surface-Enhanced Light Scattering at Single Hot Spots," *Nat. Commun.* 3 (2012): 684. DOI: 10.1038/ncomms1674

12. S. Kumar, K. Tokunaga, K. Namura, T. Fukuoka, and M. Suzuki, “Experimental Evidence of a Twofold Electromagnetic Enhancement Mechanism of Surface-Enhanced Raman Scattering,” *J. Phys. Chem. C* 124, no. 38 (2020): 21215. DOI: 10.1021/acs.jpcc.0c07930
13. J. J. Baumberg, J. Aizpurua, M. H. Mikkelsen, and D. R. Smith, “Extreme Nanophotonics from Ultrathin Metallic Gaps,” *Nat. Mater.* 18 (2019): 668. DOI: 10.1038/s41563-019-0290-y
14. T. Atay, J. H. Song, and A. V. Nurmikko, “Strongly Interacting Plasmon Nanoparticle Pairs: From Dipole−Dipole Interaction to Conductively Coupled Regime,” *Nano Lett.* 4, no. 9 (2004): 1627. DOI: 10.1021/nl049215n
15. Y. Tanaka, A. Sanada, and K. Sasaki, “Nanoscale Interference Patterns of Gap-Mode Multipolar Plasmonic Fields,” *Sci. Rep.* 2 (2012): 764. DOI: 10.1038/srep00764
16. Y. Yang, C. Gu, and J. Li, “Sub-5 nm Metal Nanogaps: Physical Properties, Fabrication Methods, and Device Applications,” *Small* 15, no. 5 (2019): 1804177. DOI: 10.1002/smll.201804177
17. Y. Li, W. Chen, X. He, *et al.*, “Boosting Light−Matter Interactions in Plasmonic Nanogaps,” *Adv. Mater.* 36, no. 49 (2024): 2405186. DOI: 10.1002/adma.202405186
18. S. Luo, B. H. Hoff, S. A. Maier, and J. C. de Mello, “Scalable Fabrication of Metallic Nanogaps at the Sub-10 nm Level,” *Adv. Sci.* 8, no. 24 (2021): 2102756. DOI: 10.1002/advs.202102756
19. P. Gu, W. Zhang, and G. Zhang, “Plasmonic Nanogaps: From Fabrications to Optical Applications,” *Adv. Mater. Interfaces* 5 (2018): 1800648. DOI: 10.1002/admi.201800648
20. Y. Chen, Z. Shu, S. Zhang, *et al.*, “Sub-10 nm Fabrication: Methods and Applications,” *Int. J. Extrem. Manuf.* 3 (2021): 032002. DOI: 10.1088/2631-7990/ac087c
21. L. Qin, Y. Huang, F. Xia, *et al.*, “5 nm Nanogap Electrodes and Arrays by Super-Resolution Laser Lithography,” *Nano Lett.* 20, no. 7 (2020): 4916. DOI: 10.1021/acs.nanolett.0c00978
22. T. Siegfried, Y. Ekinci, O. J. F. Martin, and H. Sigg, “Gap Plasmons and Near-Field Enhancement in Closely Packed Sub-10 nm Gap Resonators,” *Nano Lett.* 13, no. 11 (2013): 5449. DOI: 10.1021/nl403030g
23. V. R. Manfrinato, L. Zhang, D. Su, *et al.*, “Resolution Limits of Electron-Beam Lithography toward the Atomic Scale,” *Nano Lett.* 13, no. 4 (2013): 1555. DOI: 10.1021/nl304715p
24. S. Kaneko, S. Watanabe, S. Fujii, T. Nishino, and M. Kiguchi, “The Practical Electromagnetic Effect in Surface-Enhanced Raman Scattering Observed by the Lithographically Fabricated Gold Nanosquare Dimers,” *AIP Adv.* 10, no. 2 (2020): 025301. DOI: 10.1063/1.5126981

25. L. Zhang, X. Wang, H. Chen, C. Liu, and S. Deng, "A Planar Plasmonic Nano-Gap and Its Array for Enhancing Light-Matter Interactions at the Nanoscale," *Nanoscale* 14, no. 34 (2022): 12257. DOI: 10.1039/D2NR01282K
26. H. Duan, H. Hu, K. Kumar, Z. Shen, and J. K. W. Yang, "Direct and Reliable Patterning of Plasmonic Nanostructures with Sub-10-nm Gaps," *ACS Nano* 5, no. 9 (2011): 7593. DOI: 10.1021/nn2025868
27. D. Wang, W. Zhu, M. D. Best, J. P. Camden, and K. B. Crozier, "Directional Raman Scattering from Single Molecules in the Feed Gaps of Optical Antennas," *Nano Lett.* 13, no. 5 (2013): 2194. DOI: 10.1021/nl400698w
28. W. Zhu and K. B. Crozier, "Quantum Mechanical Limit to Plasmonic Enhancement as Observed by Surface-Enhanced Raman Scattering," *Nat. Commun.* 5 (2014): 5228. DOI: 10.1038/ncomms6228
29. X. Shi, D. Verschueren, S. Pud, and C. Dekker, "Integrating Sub-3 nm Plasmonic Gaps into Solid-State Nanopores," *Small* 14, no. 18 (2018): 1703307. DOI: 10.1002/smll.201703307
30. M. Manheller, S. Trellenkamp, R. Waser, and S. Karthäuser, "Reliable Fabrication of 3 nm Gaps Between Nanoelectrodes by Electron-Beam Lithography," *Nanotechnology* 23, no. 12 (2012): 125302. DOI: 10.1088/0957-4484/23/12/125302
31. S. Uchiyama, S. Ohki, and T. Matsuda, "A New Proximity Parameter Evaluation Method Utilizing Auxiliary Patterns for Dose Compensation," *Jpn. J. Appl. Phys.* 32, no. 12S (1993): 6028. DOI: 10.1143/JJAP.32.6028
32. S. Manakli, K. Docherty, L. Pain, *et al.*, "New Electron Beam Proximity Effects Correction Approach for 45 and 32 nm Nodes," *Jpn. J. Appl. Phys.* 45, no. 8R (2006): 6462. DOI: 10.1143/JJAP.45.6462
33. S. M. Lewis, G. A. DeRose, H. R. Alty, *et al.*, "Tuning the Performance of Negative Tone Electron Beam Resists for the Next Generation Lithography," *Adv. Funct. Mater.* 32, no. 32 (2022): 2202710. DOI: 10.1002/adfm.202202710
34. S. Yasin, D. G. Hasko, and H. Ahmed, "Comparison of MIBK/IPA and Water/IPA as PMMA Developers for Electron Beam Nanolithography," *Microelectron. Eng.* 61–62 (2002): 745. DOI: 10.1016/S0167-9317(02)00468-9
35. M. Oudich, X. Kong, T. Zhang, C. Qiu, and Y. Jing, "Engineered Moiré Photonic and Phononic Superlattices," *Nat. Mater.* 23 (2024): 1169. DOI: 10.1038/s41563-024-01950-9

36. Z. Wu, K. Chen, R. Menz, T. Nagao, and Y. Zheng, “Tunable Multiband Metasurfaces by Moiré Nanosphere Lithography,” *Nanoscale* 7, no. 48 (2015): 20391. DOI: 10.1039/C5NR05645D
37. B. Lou and S. Fan, “Tunable Frequency Filter Based on Twisted Bilayer Photonic Crystal Slabs,” *ACS Photonics* 9, no. 3 (2022): 800. DOI: 10.1021/acsphotonics.1c01263
38. Y. Tian, Y. Du, Z. Sun, *et al.*, “Plasmonic Resonances of Metallic Moiré Superlattices in the Infrared Range,” *Opt. Express* 33, no. 2 (2025): 1660. DOI: 10.1364/OE.545868
39. M. J. H. Tan, F. Freire-Fernández, and T. W. Odom, “Symmetry-Guided Engineering of Polarization by 2D Moiré Metasurfaces,” *ACS Nano* 18, no. 34 (2024): 23181. DOI: 10.1021/acsnano.4c05714
40. L. Qu, W. Wu, D. Zhang, *et al.*, “Beam Shaping by Stacked Nonlinear Moiré Metasurfaces,” *Nano Lett.* 25, no. 12 (2025): 4854. DOI: 10.1021/acs.nanolett.4c06570
41. S. Liu, S. Ma, R. Shao, *et al.*, “Moiré Metasurfaces for Dynamic Beamforming,” *Sci. Adv.* 8, no. 33 (2022): eabo1511. DOI: 10.1126/sciadv.abo1511
42. G. Hu, A. Krasnok, Y. Mazor, C.-W. Qiu, and A. Alù, “Moiré Hyperbolic Metasurfaces,” *Nano Lett.* 20, no. 5 (2020): 3217. DOI: 10.1021/acs.nanolett.9b05319
43. Z. Wu and Y. Zheng, “Moiré Chiral Metamaterials,” *Adv. Opt. Mater.* 5, no. 16 (2017): 1700034. DOI: 10.1002/adom.201700034
44. P. Wang, Y. Zheng, X. Chen, *et al.*, “Localization and Delocalization of Light in Photonic Moiré Lattices,” *Nature* 577 (2020): 42. DOI: 10.1038/s41586-019-1851-6
45. K. Dong, T. Zhang, J. Li, *et al.*, “Flat Bands in Magic-Angle Bilayer Photonic Crystals at Small Twists,” *Phys. Rev. Lett.* 126 (2021): 223601. DOI: 10.1103/PhysRevLett.126.223601
46. X.-R. Mao, Z.-K. Shao, H.-Y. Luan, S.-L. Wang, and R.-M. Ma, “Magic-Angle Lasers in Nanostructured Moiré Superlattice,” *Nat. Nanotechnol.* 16 (2021): 1099. DOI: 10.1038/s41565-021-00956-7
47. J. Guan, J. Hu, Y. Wang, M. J. H. Tan, G. C. Schatz, and T. W. Odom, “Far-Field Coupling Between Moiré Photonic Lattices,” *Nat. Nanotechnol.* 18 (2023): 514. DOI: 10.1038/s41565-023-01320-7
48. H.-B. Zhang, R.-J. Feng, and K. Ura, “Utilizing the Charging Effect in Scanning Electron Microscopy,” *Sci. Prog.* 87, no. 4 (2004): 249. DOI: 10.3184/003685004783238490

49. K. Suemori, Y. Watanabe, N. Fukuda, and S. Uemura, “Voltage Contrast in Scanning Electron Microscopy to Distinguish Conducting Ag Nanowire Networks from Nonconducting Ag Nanowire Networks,” *ACS Omega* 5, no. 22 (2020): 12692. DOI: 10.1021/acsomega.9b04222
50. H. Seiler, “Secondary Electron Emission in the Scanning Electron Microscope,” *J. Appl. Phys.* 54, no. 11 (1983): R1. DOI: 10.1063/1.332840
51. M. Gu, M. S. Hyun, M. Han, G. Kim, and Y. J. Chang, “Contact Holes in Vertical Electrode Structures Analyzed by Voltage Contrast-SEM and Conducting AFM,” *Curr. Appl. Phys.* 53 (2023): 46. DOI: 10.1016/j.cap.2023.06.003
52. A. Vijayaraghavan, S. Blatt, C. Marquardt, *et al.*, “Imaging Electronic Structure of Carbon Nanotubes by Voltage-Contrast Scanning Electron Microscopy,” *Nano Res.* 1 (2008): 321. DOI: 10.1007/s12274-008-8034-3
53. N. A. Hatab, C.-H. Hsueh, A. L. Gaddis, *et al.*, “Free-Standing Optical Gold Bowtie Nanoantenna with Variable Gap Size for Enhanced Raman Spectroscopy,” *Nano Lett.* 10, no. 12 (2010): 4952. DOI: 10.1021/nl102963g
54. J. Li, C. Chen, H. Jans, *et al.*, “300 mm Wafer-Level, Ultra-Dense Arrays of Au-Capped Nanopillars with Sub-10 nm Gaps as Reliable SERS Substrates,” *Nanoscale* 6, no. 21 (2014): 12391. DOI: 10.1039/C4NR04315D
55. K. N. Kanipe, P. P. F. Chidester, G. D. Stucky, and M. Moskovits, “Large Format Surface-Enhanced Raman Spectroscopy Substrate Optimized for Enhancement and Uniformity,” *ACS Nano* 10, no. 8 (2016): 7566. DOI: 10.1021/acsnano.6b02564
56. A. Dmitriev, C. Hägglund, S. Chen, *et al.*, “Enhanced Nanoplasmonic Optical Sensors with Reduced Substrate Effect,” *Nano Lett.* 8, no. 11 (2008): 3893. DOI: 10.1021/nl8023142
57. C. J. Orendorff, A. Gole, T. K. Sau, and C. J. Murphy, “Surface-Enhanced Raman Spectroscopy of Self-Assembled Monolayers: Sandwich Architecture and Nanoparticle Shape Dependence,” *Anal. Chem.* 77, no. 10 (2005): 3261. DOI: 10.1021/ac048176x
58. M. H. Moghaddam, S. Sharma, D. Park, and D. S. Kim, “Tuning 1D Plasmonic Gap at Nanometer Scale for Advanced SERS Detection,” *Adv. Opt. Mater.* 13 (2025): 2403021. DOI: 10.1002/adom.202403021
59. S. S. Walavalkar, P. Latawiec, A. P. Homyk, and A. Scherer, “Scalable Method for the Fabrication and Testing of Glass-Filled, Three-Dimensionally Sculpted Extraordinary Transmission Apertures,” *Nano Lett.* 14, no. 1 (2013): 311. DOI: 10.1021/nl4040576

60. K. J. Savage, M. M. Hawkeye, R. Esteban, A. G. Borisov, J. Aizpurua, and J. J. Baumberg, "Revealing the Quantum Regime in Tunnelling Plasmonics," *Nature* 491 (2012): 574. DOI: 10.1038/nature11653
61. J. A. Scholl, A. García-Etxarri, A. L. Koh, and J. A. Dionne, "Observation of Quantum Tunneling Between Two Plasmonic Nanoparticles," *Nano Lett.* 13, no. 2 (2013): 564. DOI: 10.1021/nl304078v
62. W. Zhu, R. Esteban, A. G. Borisov, *et al.*, "Quantum Mechanical Effects in Plasmonic Structures with Subnanometre Gaps," *Nat. Commun.* 7 (2016): 11495. DOI: 10.1038/ncomms11495
63. C. Lee, B. Lawrie, R. Pooser, K.-G. Lee, C. Rockstuhl, and M. Tame, "Quantum Plasmonic Sensors," *Chem. Rev.* 121, no. 8 (2021): 4743. DOI: 10.1021/acs.chemrev.0c01028